



NATIONAL TECHNICAL UNIVERSITY OF ATHENS
SCHOOL OF MECHANICAL ENGINEERING
FLUID MECHANICS DEPARTMENT

DIPLOMA THESIS

AERODYNAMIC SIMULATION OF ROTORCRAFT IN FORWARD FLIGHT USING THE PETERS-HE FINITE-STATE INFLOW MODEL

Author:
VICTORIA MALYSHKINA

Supervisor:
VASILIS RIZIOTIS

A thesis submitted in fulfillment of the requirements for the
degree of Master of Science in Mechanical Engineering

Athens,
Monday 14th October, 2024

Υπεύθυνη δήλωση για λογοκλοπή και για κλοπή πνευματικής ιδιοκτησίας:

Έχω διαβάσει και κατανοήσει τους κανόνες για τη λογοκλοπή και τον τρόπο σωστής αναφοράς των πηγών που περιέχονται στον οδηγό συγγραφής Διπλωματικών Εργασιών. Δηλώνω ότι, από όσα γνωρίζω, το περιεχόμενο της παρούσας Διπλωματικής Εργασίας είναι προϊόν δικής μου εργασίας και υπάρχουν αναφορές σε όλες τις πηγές που χρησιμοποίησα.

Οι απόψεις και τα συμπεράσματα που περιέχονται σε αυτή τη Διπλωματική εργασία είναι του συγγραφέα και δεν πρέπει να ερμηνευθεί ότι αντιπροσωπεύουν τις επίσημες θέσεις της Σχολής Μηχανολόγων Μηχανικών ή του Εθνικού Μετσόβιου Πολυτεχνείου.

Μαλισκίνα Βικτώρια

Acknowledgements

Foremost, I would like to express my deepest gratitude to my supervisor, Professor Vasilis Riziotis, for his support, invaluable advice, and guidance throughout my academic journey. I hold Professor Riziotis in the highest regard, not only as an exemplary figure in his field but also for the profound impact his teaching has had on my academic and professional development. His expertise and genuine passion for his work have been a constant source of inspiration to me.

Moreover, I am deeply appreciative of my fellow students and friends, Dimitris Moustroufis and Thanos Patsas, for their outstanding collaboration on the numerous projects we have undertaken together during our academic journey. Working with them has been a rewarding experience due to their remarkable work ethic and determination.

Furthermore, I would like to express my deep gratitude to the Libre Space Foundation, and especially to Manolis Surligas. His guidance has been very valuable for me, providing insights and feedback that have accelerated my learning and professional development in the aerospace field. As an undergraduate, working alongside someone of his expertise has been inspiring.

Lastly, I am profoundly grateful to my family for their emotional support. Their encouragement has been a source of strength during challenging times.

Abstract

This thesis focuses on the development of a versatile and efficient simulation code for the Peters-He finite-state dynamic inflow model. The inflow model will be integrated with Blade Element Theory (BET) to analyze helicopter performance in both forward flight and hover conditions. The performance of this model will be evaluated by comparing it to a free wake lifting line model, which offers higher fidelity but is computationally intensive and unsuitable for real-time applications.

The aim is to demonstrate that increasing the number of states in the Peters-He model allows for performance predictions in helicopters that closely match those of a free wake lifting line model, while significantly reducing computational demands. This makes the method potentially suitable for real-time applications, such as flight dynamics simulations and control systems assessment studies.

Although similar code models have been developed, they are often part of proprietary or restricted university code bases, limiting their accessibility. To address this significant gap, the code, and simulations developed in this thesis are made open-source, to benefit the broader academic and engineering community.

Περίληψη

Αυτή η διπλωματική εργασία επικεντρώνεται στην ανάπτυξη ενός ευέλικτου και αποδοτικού κώδικα προσομοίωσης για το δυναμικό μοντέλο αεροδυναμικής επαγωγής πεπερασμένων καταστάσεων Peters-He. Το μοντέλο για τον υπολογισμό του ομόρρου θα ενσωματωθεί με τη θεωρία Blade Element για την ανάλυση της απόδοσης ελικοπτέρων τόσο σε εμπρόσθια πτήση όσο και σε αιώρηση. Η απόδοση αυτού του μοντέλου θα συγκριθεί με ένα μοντέλο γραμμής άνωσης ελεύθερου ομόρρου, το οποίο προσφέρει υψηλότερη ακρίβεια αλλά είναι υπολογιστικά απαιτητικό και ακατάλληλο για εφαρμογές που απαιτούν υπολογισμούς σε πραγματικό χρόνο.

Ο στόχος είναι να αποδειχθεί ότι, με την αύξηση των βαθμών ελευθερίας στο μοντέλο Peters-He, είναι δυνατό να επιτευχθούν αποτελέσματα παρόμοια με αυτά του μοντέλου γραμμής άνωσης ελεύθερου ομόρρου, αλλά με σημαντικά μειωμένες υπολογιστικές απαιτήσεις. Οι μειωμένες χρονικές απαιτήσεις δύναται να καταστήσουν τον κώδικα κατάλληλο για εφαρμογές σε πραγματικό χρόνο, όπως, για παράδειγμα, υπολογισμοί δυναμικής πτήσης και αξιολόγηση συστημάτων ελέγχου.

Αν και παρόμοια υπολογιστικά μοντέλα έχουν αναπτυχθεί, δεν είναι διαθέσιμα στη γενική επιστημονική κοινότητα. Για την αντιμετώπιση αυτού του σημαντικού κενού, οι προσομοιώσεις που αναπτύχθηκαν για αυτήν τη διπλωματική εργασία είναι ανοιχτού κώδικα, με την πρόθεση να ωφεληθεί την ευρύτερη ακαδημαϊκή κοινότητα.

Contents

Acknowledgements	ii
Abstract	iii
Περίληψη	iv
1 Introduction	1
1.1 Motivation	1
1.2 Background	1
1.3 Objectives	1
1.4 Organization of the thesis	2
2 Literature review	4
3 Technical Background	8
3.1 Peters-He finite state dynamic inflow model	8
3.2 Blade element theory	12
4 Method	14
4.1 Parameters Initialization	14
4.2 General Algorithm Description	14
4.3 Influence Matrices $[\tilde{L}_{jn}^{rm}]^{c,s}$ Calculation Algorithm	14

4.4 Loading Coefficients $[\tau_n^m]^{c,s}$ Calculation Algorithm	17
5 Results	20
5.1 BO-105 helicopter model description	20
5.2 Peters-He and Free Wake Lifting Line model results comparison	20
6 Conclusions	27
Nomenclature	29
A Appendix: BO-105 helicopter polar data	30
Appendix: Εκτενής Περίληψη στα Ελληνικά	34

List of Figures

1	Blade element diagram	13
2	Basic Peters-He algorithm	15
3	Influence Matrices $[\tilde{L}_{jn}^{rm}]^{c,s}$ Calculation Algorithm	18
4	Inflow Distribution $w(\bar{r}, \psi)$ Calculation Algorithm	19
5	BO-105: Inflow distribution w_{inflow} for $\mu = 0.26$	21
6	BO-105: Normal loading coefficient distribution C_N for $\mu = 0.26$	22
7	BO-105: Local velocity distribution U for $\mu = 0.26$	22
8	BO-105: Angle of attack distribution α for $\mu = 0.26$	23
9	BO-105: Inflow distribution w_{inflow} for $\mu = 0.13$	23
10	BO-105: Normal loading coefficient distribution C_N for $\mu = 0.13$	24
11	BO-105: Local velocity distribution U for $\mu = 0.13$	24
12	BO-105: Angle of attack distribution α for $\mu = 0.13$	25
13	Results for $\mu = 0.26$ and $\bar{r} = 0.5$ as a function of azimuthal position	25
14	Results for $\mu = 0.13$ and $\bar{r} = 0.5$ as a function of azimuthal position	26
15	BO-105 : Αδιάστατη επαγομένη ταχύτητα, w_{inflow} για $\mu = 0.26$	iii
16	BO-105 : Συντελεστής κάθετης φόρτισης C_N για $\mu = 0.26$	iii
17	BO-105 : Τοπική ταχύτητα U για $\mu = 0.26$	iv

18	BO-105 : Γωνία προσβολής α για $\mu = 0.26$	iv
19	BO-105 : Αδιάστατες επαγόμενες ταχύτητες, w_{inflow} για $\mu = 0.13$	v
20	BO-105 : Συντελεστής κάθετης φόρτισης C_N για $\mu = 0.13$	v
21	BO-105 : Τοπική ταχύτητα U φορ $\mu = 0.13$	vi
22	BO-105 : Γωνία προσβολής α για $\mu = 0.13$	vi
23	Αποτελέσματα για $\mu = 0.26$ και $\bar{r} = 0.5$ ως συνάρτηση της αζιμουθιακής θέσης . .	vii
24	Αποτελέσματα για $\mu = 0.13$ και $\bar{r} = 0.5$ ως συνάρτηση της αζιμουθιακής θέσης . .	viii

List of Tables

1	First Harmonic Inflow Model Coefficients [2]	5
2	Number of shape functions per harmonic	10
3	Matrix $[L_{jn}^{rm}]^c$ for $M = 3, Q = 4$	11
4	Matrix $[L_{jn}^{rm}]^s$ for $M = 3, Q = 4$	11
5	BO-105 helicopter specifications	20
6	BO-105 helicopter operating conditions	20
7	BO-105 helicopter blade chord and twist angle distribution as a function of radius	21
8	Aerodynamic Coefficients C_L, C_D , and C_M for Mach 0.00, 0.20, and 0.40	30
9	Aerodynamic Coefficients C_L, C_D , and C_M for Mach 0.50, 0.60, and 0.70	31
10	Aerodynamic Coefficients C_L, C_D , and C_M for Mach 0.80, 0.85, and 0.90	32

1 Introduction

A helicopter is a rotorcraft that uses one or more horizontally rotating rotors to generate lift. This configuration allows the aircraft to take off and land vertically (VTOL), hover in place, and fly forward, backward, and laterally. Unlike fixed-wing aircraft, which rely on the magnitude of forward velocity to achieve liftoff, helicopters use their rotors to generate lift directly, giving them exceptional maneuverability and versatility.

This capability makes helicopters invaluable for critical missions such as rescue operations during fires, earthquakes, and floods. They can transport people to hospitals, quickly deliver medical supplies or other essentials, and land on hospital roofs to provide immediate assistance. Their ability to function in challenging or inaccessible environments significantly increases their importance in emergency response and other vital engineering applications.

1.1 Motivation

Although they are highly beneficial, helicopters presented the engineering community with exceptionally challenging problems. Their complexity arises from the rotating blades and significant mass. In general, rotor efficiency is closely tied to the taper ratio of the blades, which suggests that the blades should be long with a relatively small chord. This results in the blades experiencing very high speed and pressure variations, leading to significant dynamic loading. To address this issue, hinges and flexible blades are introduced; without these features, the blades would break under extreme loads. Thus, the hub and tips experience intense loading, leading to the formation of strong vortices that dominate the wake and interact with other blades. This interaction causes fluctuations in the aerodynamic forces produced by the rotor. Therefore, accurately modeling the induced velocity field or inflow distribution is crucial for predicting the helicopter's flight dynamics and performance.

1.2 Background

Many helicopter simulators typically use relatively simple inflow models, as obtaining a higher fidelity solution (using vortex or CFD models) for the induced velocity field is very slow with current computational capacities. High-fidelity methods provide detailed results, but are computationally expensive and time consuming. In contrast, simpler methods reduce computational costs, but do not capture essential wake characteristics. Therefore, developing a computationally efficient and relatively accurate model is vital for faster simulations needed for real-time state prediction, generating numerous flight states before take-off, or combining flight dynamics equations with control theory or machine learning techniques. For example, more sophisticated inflow models, such as the Peters-He finite-state inflow model, can offer more accurate predictions without significantly increasing computational costs. As described in [13], using it alongside Blade Element Theory can yield fast and precise predictions.

1.3 Objectives

The scope of this thesis is to develop a versatile and fast simulation code for helicopter forward flight and hover analysis using the finite-state dynamic inflow model by Peters-He [5] and Blade Element Theory (BET). The code can also be adapted for multicopters by including additional rotors in the configuration, such as quadrotors, using the Peters-He inflow model [15].

Currently, there are no open-source implementations of the Peters-He model, which made the development of this particular model especially challenging. Constructing it from the ground up was not an easy task, particularly without access to intermediate results or any existing reference code. Therefore, the goal of this thesis is to make the code developed for this thesis available on an open source platform, utilizing open source tools, so that it can be made accessible to the entire academic community.

In a nutshell, the key objectives of this thesis are the following:

1. **Develop a Versatile Simulation Code:** Create a simulation code that accurately models helicopter forward flight dynamics using the Peters-He finite-state dynamic inflow model and Blade Element Theory.
2. **Open Development:** All development stages will be documented using a git versioning system, allowing users to trace the model development step by step.
3. **Open source code:** Make the simulation code available as a free and open source package, allowing researchers and students to integrate it into their simulators or use it to compare intermediate results. This approach will allow them to concentrate on other aspects of rotorcraft design and control, such as control modeling and algorithm development, without having to develop the code for an advanced inflow model from scratch.
4. **Simulations and Validations:** Perform simulations to verify the accuracy of the developed simulation model by comparing it with an existing lifting line free wake model developed at the Aerodynamic Laboratory of the National Technical University of Athens [16] using the BO-105 helicopter.

In a nutshell, the ultimate goal is to provide an accurate and efficient open-source tool for helicopter flight dynamics inflow simulation with the Peters-He model that is accessible to researchers and developers.

1.4 Organization of the thesis

In Chapter 1, an overview of the research objectives, the importance of developing a versatile and efficient simulation code for helicopter performance analysis, and the motivations behind choosing the Peters-He model and Blade Element Theory (BET) are provided. The challenges addressed by the research and the potential impact of the open-source code are also outlined.

In Chapter 2, a comprehensive review of the literature on inflow models is presented. This includes a detailed discussion of the Pitt-Peters and Peters-He inflow models as well as the limitations of existing models.

In Chapter 3, the theoretical foundations of the Peters-He model and its integration with the Blade Element Theory are discussed. The chapter covers the mathematical formulations used, the derivation of key equations, and the iterative methods applied to resolve the interdependencies between the inflow distribution and the blade loading.

In Chapter 4, the development and implementation of the simulation code are detailed. This includes software architecture, coding strategies, and the use of open source tools. The challenges encountered during implementation and how they were overcome are also discussed.

In Chapter 5, the validation of the developed simulation code is discussed. The chapter presents the results of the simulations using the BO-105 helicopter and compares the performance of the Peters-He model with a free wake lifting line model to evaluate accuracy and fidelity of the developed codebase.

In Chapter 6, the key findings of the thesis are summarized. The chapter highlights the contributions made to the field of helicopter performance analysis and reflects on the importance of open source code. Suggestions are also provided for future research.

2 Literature review

As rotor system models have advanced, it has become evident that aerodynamic models must also be more detailed. A crucial aspect of helicopter aerodynamics is the induced velocity in the main rotors, which refers to the airflow generated by the rotating blades. Accurately modeling the distribution of induced velocity is essential for predicting the aerodynamic forces and moments acting on the rotor, as it significantly influences the lift distribution along the blades and, consequently, the overall performance of the helicopter.

In the early stages of developing inflow models, a uniform induced velocity model, based on momentum theory, was utilized [9]. This approach offered simplicity and reduced computation time, but significantly compromised accuracy, especially under certain conditions.

Promptly, it became clear that different helicopter flight conditions, such as hover, vertical, low-speed, and high-speed forward flight, required different modeling approaches. For instance, while the assumption of uniform inflow was adequate for hovering, it proved to be particularly inaccurate for forward flight, highlighting the need for a more sophisticated and detailed approach. This section will detail how researchers addressed these issues in their models while maintaining low computational costs [2].

In particular, advances in finite-state inflow models and computational power have facilitated more realistic modeling of inflow variations and rotor wake dynamics. A finite-state inflow model is a mathematical modeling approach used to describe the velocity field induced by the rotor wake. This model reduces the complex, time-varying nature of wake dynamics into a simplified form that still effectively captures the key aspects of the induced flow, but with a limited number of states or degrees of freedom. This enhancement is important as it improves the accuracy of helicopter models, leading to better predictions of helicopter performance and efficiency, as well as more accurate and versatile control models.

Thus, after initially relying on the uniform induced velocity assumption, the first non-uniform finite-state inflow model was developed. Specifically, in 1926, Glauert [8] introduced a straightforward non-uniform first-harmonic inflow model to address the discrepancies between experimentally observed and theoretically calculated data. This model produces an induced velocity field defined in Eq.(1).

$$w(\bar{r}, \psi) = w_0(1 + \bar{r}K_c \cos \psi) \quad (1)$$

Subsequently, Wheatley [22] built on Glauert's work by aligning the gradient value $K_c = 0.5$ with flight test data from an autogyro. He concluded that the motion of the blade was highly dependent on the distribution of induced velocities across the rotor disc. Wheatley's findings highlighted the importance of accurately determining the induced flow for accurate helicopter flight modeling.

In 1945, Coleman [3] analytically determined the parameter K_c . Specifically, he used a cylindrical wake model. In the end a simple Eq.(2) was derived.

$$K_c = \tan(\chi/2) \quad (2)$$

Over the years, several authors have developed other formulae for K_c and K_s . Some of these, recast as an explicit function of wake skew angle, are summarized in Table (1).

In 1945, Drees [6] proposed that the circulation varies sinusoidally with azimuth and introduced the parameter K_s in the inflow calculation Eq.(3).

$$w(\bar{r}, \psi) = w_0[1 + \bar{r}(K_c \cos \psi + K_s \sin \psi)] \quad (3)$$

Year	Author(s)	K_c	K_s
1945	Coleman et al. [3]	$\tan(\chi/2)$	0
1949	Drees [6]	$\frac{4}{3}(1 - 1.8\mu^2) \tan(\chi/2)$	-2μ
1959	Payne [18]	$\frac{(4/3) \tan(\chi)}{1.2 + \tan(\chi)}$	0
1979	Blake and White [23]	$\sqrt{2} \sin(\chi)$	0
1981	Pitt and Peters [21]	$\frac{15\pi}{32} \tan(\chi/2)a$	0
1981	Howlett [11]	$\sin^2(\chi)$	0

Table 1: First Harmonic Inflow Model Coefficients [2]

Subsequently, a new era in inflow models began as the first dynamic inflow model was introduced. In 1953, Carpenter and Fridovich [1] proposed the first dynamic inflow model to investigate the transient rotor thrust and the inflow variation in a maneuvering flight.

In 1971, Curtiss and Shupe [4] extended Glauert's model to include inflow perturbations from pitching and rolling moments in hingeless rotors.

After almost two decades, in 1972, the work on dynamic inflow models was continued by Ormiston and Peters [17]. A first harmonic inflow model was developed using a simple vortex theory, where they expressed the dynamic inflow model in state-space form for the first time and used a Fourier series to model the inflow distribution. Their model is briefly summarized in [13].

Specifically, the inflow at any point on the rotor disk was modeled as a combination of uniform, longitudinal, and lateral components, with the inflow dependent on the position on the disk (given by the radial location r and the azimuthal angle ψ). This relation is represented by Eq.(4).

$$\lambda = \lambda_0 + \lambda_s r \sin \psi + \lambda_c r \cos \psi \quad (4)$$

The coefficients λ_0 , λ_s , and λ_c are affected by the aerodynamic forces that act on the rotor, such as lift C_T , roll C_R , and pitch moment C_M . The relationship between inflow and aerodynamic loads can be described using parameters like the lift curve slope and rotor solidity, as outlined in Eq.(5).

$$\begin{bmatrix} d\lambda_0 \\ d\lambda_s \\ d\lambda_c \end{bmatrix} = \begin{bmatrix} \frac{d\lambda_0}{d(C_T/C_{l\alpha}\sigma)} & \frac{d\lambda_0}{d(C_R/C_{l\alpha}\sigma)} & \frac{d\lambda_0}{d(C_M/C_{l\alpha}\sigma)} \\ \frac{d\lambda_s}{d(C_T/C_{l\alpha}\sigma)} & \frac{d\lambda_s}{d(C_R/C_{l\alpha}\sigma)} & \frac{d\lambda_s}{d(C_M/C_{l\alpha}\sigma)} \\ \frac{d\lambda_c}{d(C_T/C_{l\alpha}\sigma)} & \frac{d\lambda_c}{d(C_R/C_{l\alpha}\sigma)} & \frac{d\lambda_c}{d(C_M/C_{l\alpha}\sigma)} \end{bmatrix} \begin{bmatrix} d(C_T/C_{l\alpha}\sigma) \\ d(C_R/C_{l\alpha}\sigma) \\ d(C_M/C_{l\alpha}\sigma) \end{bmatrix} \quad (5)$$

Here, r and ψ denote the radial location and azimuthal angle, respectively. The coefficients λ_0 , λ_s , and λ_c are considered linear combinations of the first-order effects of aerodynamic loads, including rotor lift C_T , roll moment C_R , and pitch moment C_M . This relationship is captured in Eq.(4), where $\{d\lambda\}$ represents changes in inflow coefficients, $C_{l\alpha}$ is the slope of the lift curve, and σ is the rotor solidity.

Consequently, the governing equation becomes $\{d\lambda\} = [L]\{dF\}$, and the task is to determine the values in the matrix $[L]$. Ormiston and Peters' method for solving $[L]$ relied on the assumption of a simple non-uniform inflow, utilizing the horseshoe vortex method that connects the longitudinal component of the induced velocity to the circulation strength Γ . This relationship is described in Eq.(5).

$$v_c = \frac{\Gamma}{\pi R^2} \quad (5)$$

The force distribution was calculated as $T = 2\rho U_\infty \Gamma R$, which was then used to derive the thrust, roll moment, and pitch moment coefficients in the matrix. With the known values of $\{d\lambda\}$ and $\{dF\}$, the elements within $[L]$ could easily be determined.

Compared with the experimental data, the simple inflow model was found to only predict general trends in the responses of the blades. However, the empirical induced flow model provided significantly better results. As a result, researchers recognized the necessity of developing a more precise dynamic inflow model that would be built upon this generalized blade response equation.

In 1974, Peters [20] extended prior research by creating a more comprehensive dynamic inflow model for hovering, integrating the effects of unsteady inflow into Eq.(6).

$$dF = 2\Omega R v \dot{m} + 2\Omega R \dot{v} dm \quad (6)$$

Here, \dot{v} represents the time derivative of the inflow velocity. With this addition, the generalized harmonic response of the blade can be expressed as Eq.(7).

$$[M] \begin{bmatrix} d\dot{\lambda}_0 \\ d\dot{\lambda}_c \\ d\dot{\lambda}_s \end{bmatrix} + [V][L]^{-1} \begin{bmatrix} d\lambda_0 \\ d\lambda_c \\ d\lambda_s \end{bmatrix} = \begin{bmatrix} d(C_T/C_{l\alpha}\sigma) \\ d(C_R/C_{l\alpha}\sigma) \\ d(C_M/C_{l\alpha}\sigma) \end{bmatrix} \quad (7)$$

Peters' model was validated against wind tunnel data and demonstrated strong performance in hovering conditions. However, it was less suitable for forward flight. Despite incorporating unsteady inflow into the generalized response equation, theoretical inflow models failed to match the accuracy of empirical models for blade response. Consequently, research has shifted toward refining theoretical dynamic inflow models instead of continuing to explore blade aeroelasticity.

Subsequently, the Pitt and Peters model [21], introduced in 1981, became an important tool for analyzing rotorcraft aerodynamics. This model is applicable for both forward flight and hovering, as it includes unsteady aerodynamic effects. It has found extensive application in stability and control analysis, as well as in real-time aerodynamic simulations. Their theory was developed to derive the matrices L and M in Eq.(7) from a theoretical point of view.

However, the Pitt-Peters model has a limitation: it primarily focuses on low aerodynamic frequencies, since it only includes the first two harmonics of the blade response. This focus on low frequencies makes it less suitable for studying high-frequency dynamics, such as vibrations in aeroelastic systems, which are critical for helicopter design and analysis. Furthermore, the model was shown to be not reliable for the wake skew angle $\alpha < 10^\circ$, which is the case for high-speed forward flights [13]. Lastly, the model using the actuator disk theory could not include the finite number of blades.

In 1989, the Peters-He finite-state method was introduced [5]. It significantly advanced the Pitt-Peters dynamic inflow model by allowing for more accurate representation of rotor wake dynamics. This new approach expanded the model to handle a range of wake skew angles from 0° to 90° , incorporate higher harmonic blade responses, and account for a finite number of blades. Specifically, this method used a discretization of the blade sections, with each section's inflow state calculated iteratively. Moreover, it incorporated three-dimensional potential flow equations, which allowed the derivation of closed-form solutions. Furthermore, the fidelity of the model is designed to improve significantly by increasing the number of states, with up to a hundred used in high-fidelity simulations [12]. These inflow states are expressed azimuthally using Fourier series and radially through Legendre functions, with a fully closed-form solution derived for practical use.

It is well worth mentioning that in 1991 Peters and He compared their model with experimental data [19]. Specifically, the model predictions demonstrated strong agreement with the

laser velocimeter measurements of inflow distribution performed in the US Army laboratory [7]. This validation confirmed the accuracy of the Peters-He model under different operating conditions, establishing it as a reliable tool for analyzing the performance of the rotorcraft in both hover and forward flight.

Lastly, the model was incorporated into flight dynamics codes such as FLIGHTLAB and RCAS, where it demonstrated practical effectiveness, receiving positive feedback from test pilots.

3 Technical Background

3.1 Peters-He finite state dynamic inflow model

This theory is initially presented in [5], and after being structured and summarized in [13], [10], and [12].

The Peters-He theory begins with the continuity and momentum equations for an incompressible potential flow across the rotor disk in Eq.(8).

$$\begin{aligned} q_{i,i} &= 0 \\ \dot{q}_i - V_\infty q_{i,\xi} &= -\Phi \end{aligned} \quad (8)$$

In this formulation, q represents the velocity component, where the first equation captures the spatial derivatives of these velocity components. The second equation reflects the local acceleration, \dot{q} , combined with the convective acceleration in the freestream direction, denoted as ξ . The term Φ is the non-dimensional pressure across the rotor disk, which essentially represents the momentum equation in the absence of viscous effects.

The pressure Φ in the momentum equation can be decomposed into two parts: The component due to momentum flux (Φ^V) and the component due to acceleration (Φ^A). The same holds for differentiating with respect to the variable i .

$$\begin{aligned} \Phi &= \Phi^V + \Phi^A \\ \Phi &= V_\infty q_{i,\xi} + (-\dot{q}_i) \\ \Phi_i &= \Phi_i^V + \Phi_i^A \end{aligned} \quad (9)$$

This decomposition helps to separate the effects of steady and unsteady aerodynamics. Each component satisfies the Laplace equation, which ensures that the flow remains irrotational.

To solve the Laplace equation, the separation of variables technique is applied. This method breaks down the problem into simpler parts by assuming that the solution can be written as a product of functions, each depending on a single coordinate.

Specifically, the pressure discontinuity across the rotor disk, responsible for generating lift, is modeled using the Kinner potential functions.

The solution for the acceleration potential Φ involves associated Legendre functions $P_n^m(\nu)$ and $Q_n^m(i\eta)$ of the first and second kinds. These functions are used when solving partial differential equations in spherical or ellipsoidal coordinates.

The general solution for the acceleration potential is given in Eq.(10)

$$\Phi = \sum_{n,m;n>m,n+m \text{ odd}} P_n^m(\nu) Q_n^m(i\eta) [C_n^m \cos \mu\psi + D_n^m \sin \mu\psi] \quad (10)$$

Here, ν, η, ψ are ellipsoidal coordinates and C_n^m and D_n^m are arbitrary time-dependent coefficients.

The lift generated by the rotor is calculated by evaluating the difference in pressure between the upper and lower surfaces of the rotor blades. The resulting expression for the lift involves summing up contributions from the Legendre functions and the pressure coefficients τ_n^{mc} and τ_n^{ms} , which represent the cosine and sine components of the inflow.

The method then connects the inflow distribution to the blade loads by integrating the pressure term Φ^V along the freestream direction, the inflow distribution can be expressed as a function of azimuthal harmonics and radial distribution functions.

$$w(\bar{r}, \psi, t) = \sum_{r=0}^{\infty} \sum_{j=r+1, r+3, \dots}^{\infty} \phi_j^r(\bar{r}) [\alpha_j^r(t) \cos(r\psi) + \beta_j^r(t) \sin(r\psi)] \quad (11)$$

This Eq.(11) captures the inflow as a series expansion in terms of azimuthal and radial functions, with coefficients α_j^r and β_j^r that depend on time.

This equation indicates that the inflow, which depends on the radial and azimuthal position, can be expressed using the induced flow coefficients α_j^r and β_j^r . These coefficients are presented in vector form.

The induced flow coefficients can be calculated from the Eq.(12). Note that $\{\alpha_j^r\}'$ and $\{\beta_j^r\}'$ are time derivatives. These equations relate the induced flow coefficients τ_m^n to the rotor loading coefficients through constant matrices, for a specific flight condition, $[L^c]$, $[L^s]$, and $[M]$.

$$\begin{aligned} [M] \begin{bmatrix} \vdots \\ \{\alpha_j^r\}' \\ \vdots \end{bmatrix} + [L^c]^{-1} \begin{bmatrix} \vdots \\ \{\alpha_j^r\} \\ \vdots \end{bmatrix} &= \begin{bmatrix} \vdots \\ \{\tau_m^n\}^c \\ \vdots \end{bmatrix} \\ [M] \begin{bmatrix} \vdots \\ \{\beta_j^r\}' \\ \vdots \end{bmatrix} + [L^s]^{-1} \begin{bmatrix} \vdots \\ \{\beta_j^r\} \\ \vdots \end{bmatrix} &= \begin{bmatrix} \vdots \\ \{\tau_m^n\}^s \\ \vdots \end{bmatrix} \end{aligned} \quad (12)$$

The terms $\{\alpha_j^r\}'$ and $\{\beta_j^r\}'$, along with the matrix $[M]$, are used to introduce coefficients for unsteady flow conditions. These coefficients are essential for accurately modeling scenarios such as start-up, acceleration, and maneuvering. However, since this thesis is centered on trimmed forward flight, which is treated as quasi-static, the unsteady terms can be neglected.

Consequently, the equations are rearranged as presented in Eq.(30)-(31).

$$w(\bar{r}, \psi) = \sum_{r=0}^{\infty} \sum_{j=r+1, r+3, \dots}^{\infty} \phi_j^r(\bar{r}) [\alpha_j^r \cos(r\psi) + \beta_j^r \sin(r\psi)] \quad (13)$$

$$\begin{aligned} \begin{bmatrix} \vdots \\ \{\alpha_j^r\} \\ \vdots \end{bmatrix} &= [L_{jn}^{rm}]^c \begin{bmatrix} \vdots \\ \{\tau_m^n\}^c \\ \vdots \end{bmatrix} \\ \begin{bmatrix} \vdots \\ \{\beta_j^r\} \\ \vdots \end{bmatrix} &= [L_{jn}^{rm}]^s \begin{bmatrix} \vdots \\ \{\tau_m^n\}^s \\ \vdots \end{bmatrix} \end{aligned} \quad (14)$$

This means that an explicit solution can be found for the induced velocity coefficients by finding the inverse of the matrix $[L]$.

The radial shape function $\phi(\bar{r})$ is defined in Eqs.(15)-(16). It depends only on the non-dimensional radial position and a specific polynomial and harmonic number j and r , which is selected by the designer, depending on how much states one wants to use.

$$\phi_j^r(\bar{r}) = \sqrt{(2j+1)H_j^r} \sum_{q=r, r+2, \dots}^{j-1} \bar{r}^q \frac{(-1)^{(q-r)/2} (j+q)!!}{(q-j)!! (q+r)!! (j-q-1)!!} \quad (15)$$

$$H_j^r = \frac{(j+q-1)!! (j-q-1)!!}{(q-j)!! (q+r)!!} \quad (16)$$

In Eq.(31), harmonic numbers, denoted by r and m , correspond to different modes of oscillation within the rotor system, where r relates to the induced velocity coefficients and m to rotor loading coefficients. These harmonic numbers facilitate the decomposition of the complex inflow pattern into simpler sinusoidal components that capture the sine and cosine waves.

Furthermore, the polynomial coefficients j and n represent the indices of the shape functions within each harmonic, reflecting how inflow or loading varies along the radial position of the rotor blade.

The matrix $[L]$ is subdivided into smaller submatrices corresponding to specific harmonic combinations of r and m . The matrix structure allows the exponent of each element to indicate its submatrix grouping, with cosine terms represented by $[L_{jn}^{rm}]^c$ and sine terms represented by $[L_{jn}^{rm}]^s$. This separation facilitates independent tracking of contributions from the cosine and sine components in the overall inflow and loading pattern. The indexing for the harmonic numbers r and m follows a specific pattern: the cosine terms are indexed with $r = 0, 1, 2, 3, \dots$ and $m = 0, 1, 2, 3, \dots$, while the sine terms start from $r = 1, 2, 3, \dots$ and $m = 1, 2, 3, \dots$. The polynomial indices j and n increase by 2 (e.g., 1, 3, 5, ...), corresponding to the harmonic pairs (r, m) . This organized matrix structure is essential for efficiently solving the system of equations that govern induced flow and rotor loading.

As noted previously, the designer selects the maximum number of harmonics and the number of shape functions per harmonic. However, to ensure accurate predictions while keeping computational costs low, Peters and He recommended choosing these values based on the guidelines provided in Table (2).

Max Polynomial Q of \bar{r}	Max Harmonic Number M									Total inflow states
	0	1	2	3	4	5	6	7	8	
0	1									1
1	1	1								3
2	2	1	1							6
3	2	2	1	1						10
4	3	2	2	1	1					15
5	3	3	2	2	1	1				21
6	4	3	3	2	2	1	1			28
7	4	4	3	3	2	2	1	1		36
8	5	4	4	3	3	2	2	1	1	45

Table 2: Number of shape functions per harmonic

The variable Q corresponds to the highest power $(j-1)$ of the dimensionless radial parameter \bar{r} , which appears in Eq.(15). The variables m and r represent the harmonic numbers, with M being the maximum required number of harmonics. These numbers serve as parameters within the program.

An example of the $[L_{jn}^{rm}]$ matrices for $M = 3$ and $Q = 4$ is shown in Tables (3)-(4).

The matrices $[L]$ can be written as:

$$\begin{aligned} [L]^c &= [\tilde{L}]^c [\tilde{V}]^{-1} \\ [L]^s &= [\tilde{L}]^s [\tilde{V}]^{-1} \end{aligned} \tag{17}$$

where $[\tilde{L}]$ will be calculated based on Eq.(18).

L_{11}^{00}	L_{13}^{00}	L_{15}^{00}	L_{12}^{01}	L_{14}^{01}	L_{13}^{02}	L_{15}^{02}	L_{14}^{03}
L_{31}^{00}	L_{33}^{00}	L_{35}^{00}	L_{32}^{01}	L_{34}^{01}	L_{33}^{02}	L_{35}^{02}	L_{34}^{03}
L_{51}^{00}	L_{53}^{00}	L_{55}^{00}	L_{52}^{01}	L_{54}^{01}	L_{53}^{02}	L_{55}^{02}	L_{54}^{03}
L_{21}^{10}	L_{23}^{10}	L_{25}^{10}	L_{22}^{11}	L_{24}^{11}	L_{23}^{12}	L_{25}^{12}	L_{24}^{13}
L_{41}^{10}	L_{43}^{10}	L_{45}^{10}	L_{42}^{11}	L_{44}^{11}	L_{43}^{12}	L_{45}^{12}	L_{44}^{13}
L_{31}^{20}	L_{33}^{20}	L_{35}^{20}	L_{32}^{21}	L_{34}^{21}	L_{33}^{22}	L_{35}^{22}	L_{34}^{23}
L_{51}^{20}	L_{53}^{20}	L_{55}^{20}	L_{52}^{21}	L_{54}^{21}	L_{53}^{22}	L_{55}^{22}	L_{54}^{23}
L_{41}^{30}	L_{43}^{30}	L_{45}^{30}	L_{42}^{31}	L_{44}^{31}	L_{43}^{32}	L_{45}^{32}	L_{44}^{33}

Table 3: Matrix $[L_{jn}^{rm}]^c$ for $M = 3, Q = 4$

L_{22}^{11}	L_{24}^{11}	L_{23}^{12}	L_{25}^{12}	L_{24}^{13}
L_{42}^{11}	L_{44}^{11}	L_{43}^{12}	L_{45}^{12}	L_{44}^{13}
L_{32}^{21}	L_{34}^{21}	L_{33}^{22}	L_{35}^{22}	L_{34}^{23}
L_{52}^{21}	L_{54}^{21}	L_{53}^{22}	L_{55}^{22}	L_{54}^{23}
L_{42}^{31}	L_{44}^{31}	L_{43}^{32}	L_{45}^{32}	L_{44}^{33}

Table 4: Matrix $[L_{jn}^{rm}]^s$ for $M = 3, Q = 4$

$$\begin{aligned}
[\tilde{L}_{jn}^{0m}]^c &= X^m [\Gamma_{jn}^{0m}] \\
[\tilde{L}_{jn}^{rm}]^c &= \left(X^{|m-r|} + (-1)^l X^{m+r} \right) [\Gamma_{jn}^{rm}] \\
[\tilde{L}_{jn}^{rm}]^s &= \left(X^{|m-r|} - (-1)^l X^{m+r} \right) [\Gamma_{jn}^{rm}]
\end{aligned} \tag{18}$$

where $l = \min(r, m)$ and

$$\begin{aligned}
X &= \tan \left(\left| \frac{\chi}{2} \right| \right) \\
\chi &= \arctan \left(\left| \frac{\mu}{\lambda} \right| \right)
\end{aligned} \tag{19}$$

$$\begin{aligned}
\Gamma_{jn}^{rm} &= \frac{(-1)^{(n+j-2r)/2}}{\sqrt{H_n^m H_j^r}} \frac{2\sqrt{(2n+1)(2j+1)}}{(j+n)(j+n+2)[(j-n)^2-1]}, \text{ for } r+m \text{ even} \\
\Gamma_{jn}^{rm} &= \frac{\pi}{\sqrt{H_n^m H_j^r}} \frac{\text{sign}(r-m)}{(2n+1)(2j+1)}, \text{ for } r+m \text{ odd, } |j-1| = 1 \\
\Gamma_{jn}^{rm} &= 0, \text{ for } r+m \text{ odd, } |j-1| \neq 1
\end{aligned} \tag{20}$$

The diagonal matrix $[\tilde{V}]$ includes non-dimensional velocity terms $[\tilde{V}_n^m]$. Specifically, when $m = 0$, $[\tilde{V}_n^m] = V_T$, and when $m \neq 0$, $[\tilde{V}_n^m] = V$. These velocity terms are detailed in Eq.(21).

$$\begin{aligned}
V_T &= \sqrt{\mu^2 + \lambda^2} \\
V &= \frac{\mu^2 + (\lambda + \lambda_m)\lambda}{\sqrt{\mu^2 + \lambda^2}}
\end{aligned} \tag{21}$$

Here, λ represents the total non-dimensional inflow, which consists of two components: one from the forward velocity λ_f , and another from the momentum that produces the thrust λ_m .

This component can be determined using the Eq.(23), derived from the theory of uniform inflow.

$$\begin{aligned}\lambda &= \lambda_f + \lambda_m \\ \lambda_f &= \frac{V_\infty \sin(\alpha_{\text{shaft}})}{\Omega R}\end{aligned}\quad (22)$$

The mean inflow λ_m can be determined using Eq.(23), derived from the theory of uniform inflow.

$$\lambda_m = \sqrt{3}\lambda_0 \quad (23)$$

The coefficient λ_0 is calculated using momentum theory and a Newton-Raphson iterative procedure. The iteration scheme is presented in Eq.(24).

$$\begin{aligned}\lambda_0^{n+1} &= \lambda_0^n - \frac{f(\lambda)}{f'(\lambda)} \\ f(\lambda_0) &= \lambda_0 - \mu \tan(\alpha_{\text{shaft}}) - \frac{C_T}{2\sqrt{\mu^2 + \lambda_0^2}} \\ f'(\lambda_0) &= 1 + \frac{C_T}{2}(\mu^2 + \lambda_0^2)^{-3/2}\lambda_0\end{aligned}\quad (24)$$

The loading coefficient matrices referenced in Eq.(12) and Eq.(31) are determined using Eq.(25). Here, q denotes the blade index corresponding to azimuthal positions, while i represents the index of the blade element corresponding to the radial positions. The normal force acting on the rotor element, L_i^q , depends on both the radial and azimuthal positions. The shape function used is the same as in Eq.(15), but with r and j replaced by m and n , respectively.

$$\begin{aligned}\tau_n^{0c} &= \frac{1}{2\pi\rho\Omega^2 R^4} \sum_{q=1}^{N_q} \left[\sum_{i=1}^{N_i} L_i^q \phi_n^m(\bar{r}_i) \right] \\ \tau_n^{mc} &= \frac{1}{\pi\rho\Omega^2 R^4} \sum_{q=1}^{N_q} \left[\sum_{i=1}^{N_i} L_i^q \phi_n^m(\bar{r}_i) \right] \cos(m\psi) \\ \tau_n^{ms} &= \frac{1}{\pi\rho\Omega^2 R^4} \sum_{q=1}^{N_q} \left[\sum_{i=1}^{N_i} L_i^q \phi_n^m(\bar{r}_i) \right] \sin(m\psi)\end{aligned}\quad (25)$$

3.2 Blade element theory

The normal blade sectional force in Eq.(25) is calculated using the Blade Element Theory.

Calculating the normal sectional force of the blade, as required in Eq.(25), is performed using the Blade Element Theory. The blade section, along with local velocities and forces, is depicted in Fig. (1).

Based on Fig. (1), the angle of attack is calculated by Eq. (26).

$$\alpha = \theta_{\text{tw}} - \phi = \theta_{\text{tw}} - \tan^{-1} \left(\frac{U_P}{U_T} \right) \quad (26)$$

Thus, the tangential velocity U_T , the perpendicular velocity U_P and the freestream velocity U , all derived from the dynamic inflow model, are expressed by Eq.(27).

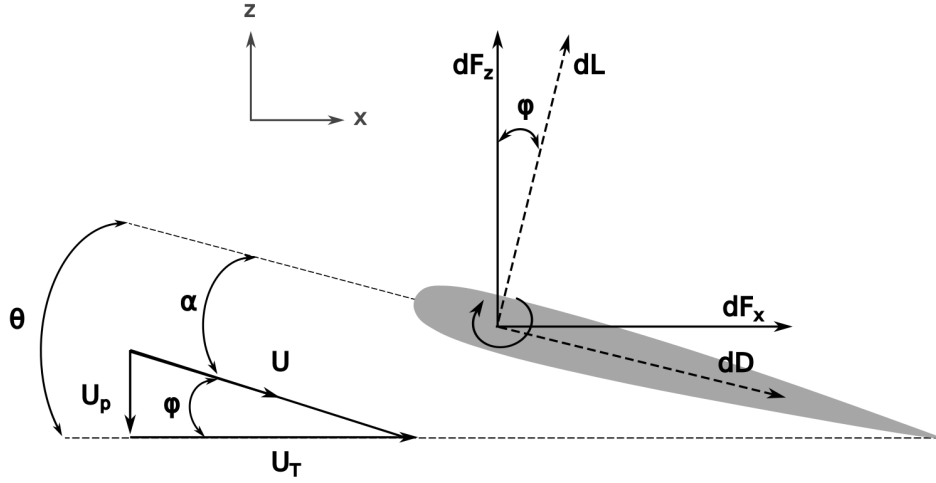


Figure 1: Blade element diagram

$$\begin{aligned}
 U_T(r, \psi) &= \Omega r + V_\infty \sin \psi \\
 U_P(r, \psi) &= (\lambda_c + w(r, \psi))\Omega R + r\dot{\beta}(\psi) + \mu\Omega R\dot{\beta}(\psi) \cos \psi \\
 U(r, \psi) &= \sqrt{U_P(r, \psi)^2 + U_T(r, \psi)^2}
 \end{aligned} \tag{27}$$

Consequently, the normal force dF_z and the tangential force dF_x acting on the blade section can be calculated using Eq.(28). For the sake of simplicity, the tip and root losses are neglected.

$$\begin{aligned}
 dF_z &= dL \cos \phi - dD \sin \phi = L_i^q \\
 dF_x &= dL \sin \phi + dD \cos \phi
 \end{aligned} \tag{28}$$

The lift dL and drag dD forces per unit length are derived from the polar data of the airfoil, as indicated in Eq.(29).

$$dL = \frac{1}{2}\rho U^2 c C_l(\alpha) dr \quad dD = \frac{1}{2}\rho U^2 c C_d(\alpha) dr \tag{29}$$

Since polar data usually only cover angles of attack up to the stall point, rotor blades in forward flight may encounter higher angles due to effects like up-wash and reverse flow. To address this, an extrapolation method is used to estimate the lift and drag coefficients in a 360 degree range of angles of attack.

4 Method

In general, it is important to note that Object-Oriented Programming (OOP) was used in the creation of the simulation source code. It was done to improve code organization, reusability, and maintainability. By encapsulating related variables and methods into classes, the code becomes modular and easier to manage. This approach also allows reuse of common functionality and makes it easier to extend the simulation by adding new features or components in the future.

4.1 Parameters Initialization

At the beginning of the simulation, the geometry and operating conditions are parsed and wrapped into class variables. In addition, some simple preliminary calculations required for the simulation are performed.

4.2 General Algorithm Description

The algorithm described below is visualized in Figure 2.

The simulation begins with the calculation of uniform inflow using simple Blade Element Theory, as described by Eqs. 26-29. Initially, the program assumes a value of $\lambda_0 = 0.01$. It is important to initialize this parameter with a reasonable value to avoid convergence issues and accelerate the overall process.

Next, uniform inflow is assumed across all radial and azimuthal positions, and the loading is calculated based on known velocities. Once the thrust coefficient, C_T , is determined, the updated value of λ_0 is found using the Newton-Raphson method, as described in Eq. 24. The process then repeats, recalculating C_T with the new λ_0 and continues until convergence is achieved.

The Newton-Raphson method usually converges rapidly, requiring fewer than 20 iterations. However, if the iteration count exceeds this limit, the initial guess may be unsuitable as the algorithm is sensitive to initial conditions. A possible solution to this problem is the relaxation technique.

Once the uniform inflow solution is obtained, the influence matrices, $[\tilde{L}_{jn}^{rm}]^{c,s}$, are calculated. These matrices, based on the mean inflow value, are computed only once and do not require further recalculations.

With the converged uniform inflow solution, the loading coefficients, $[\tau_n^{mc,s}]$, can then be calculated. These coefficients are used to iteratively compute the inflow distribution $w(\bar{r}, \psi)$.

In the following sections, a more in-depth discussion of the basic algorithm components will be provided. However, no detailed information on the uniform inflow calculation using simple BEM theory will be provided, as it primarily involves two loops iterating through all radial and azimuthal positions to compute the element velocities and loads, as outlined in the Eqs. 26-29. This process is straightforward. The choice of radial positions is up to the designer, with increased discretization improving accuracy at the expense of additional computational time. The azimuthal positions correspond to the blade locations within the rotor's rotating frame.

4.3 Influence Matrices $[\tilde{L}_{jn}^{rm}]^{c,s}$ Calculation Algorithm

The calculation of $[\tilde{L}_{jn}^{rm}]^{c,s}$ is performed only once, immediately after the uniform inflow reaches convergence.

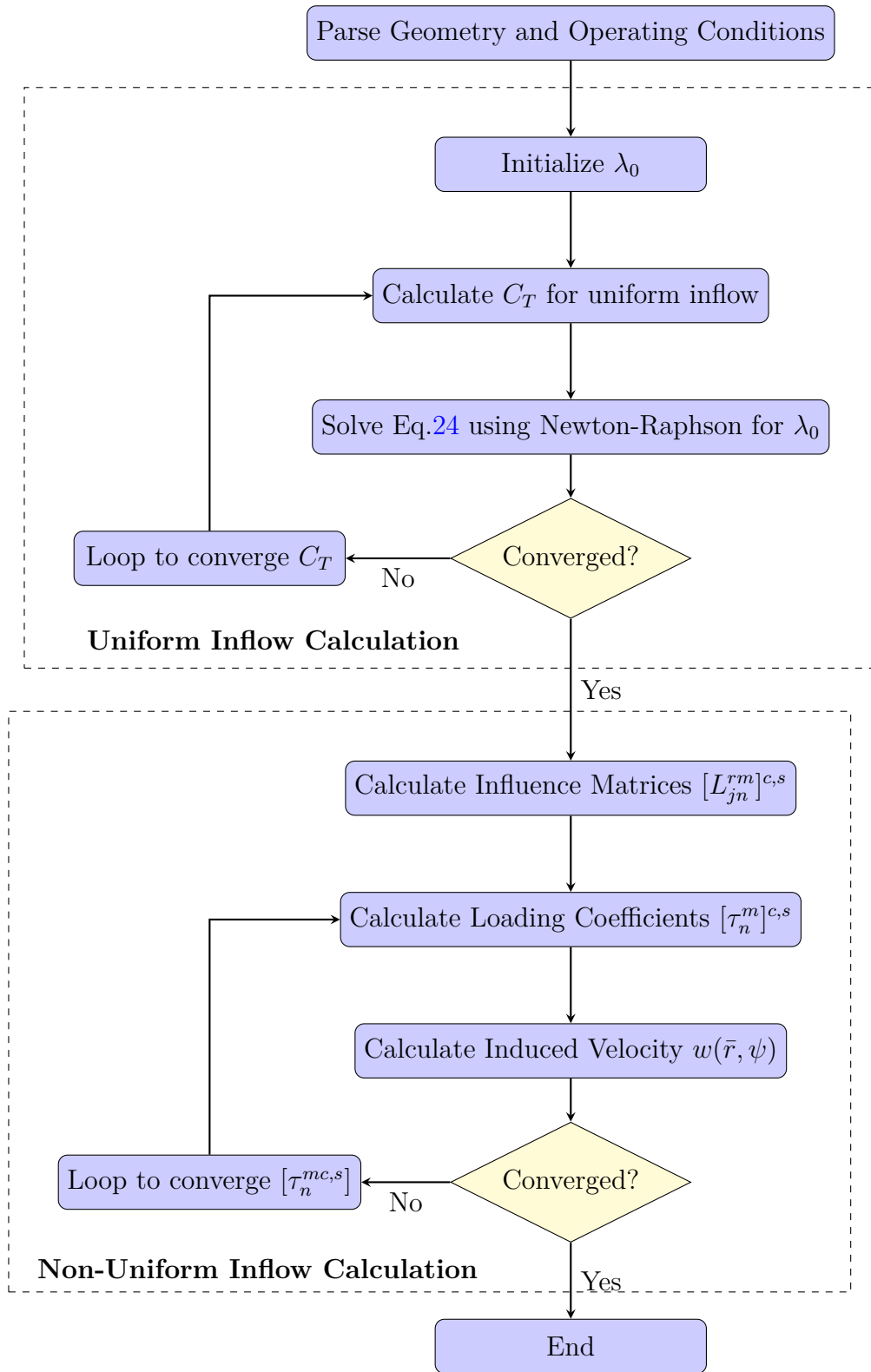


Figure 2: Basic Peters-He algorithm

The first step is to calculate the wake skew angle, χ , which serves as the primary variable for determining the elements of the matrices $[\tilde{L}_{jn}^{rm}]^{c,s}$.

To aid in the calculation of the matrix elements, a helper vector is introduced, referred to as the "shape vector." There are two types of shape vectors: the cosine shape vector and the

sine shape vector, denoted as $\mathbf{v}_{\text{shape},c}$ and $\mathbf{v}_{\text{shape},s}$, respectively.

These vectors are defined using Table 2, which correlates the row indexed by the polynomial number Q with the columns ranging from 0 to M for the harmonic number in $\mathbf{v}_{\text{shape},c}$, and from 1 to M for $\mathbf{v}_{\text{shape},s}$.

For example, when $M = Q = 3$:

$$\mathbf{v}_{\text{shape},c} = [2 \ 2 \ 1 \ 1]^T$$

$$\mathbf{v}_{\text{shape},s} = [2 \ 1 \ 1]^T$$

These vectors are derived from the user inputs for M and Q , which are stored as constants in the singleton initialization class, along with the operating conditions and rotor geometry, as mentioned above and used throughout the simulation. The size of the loading matrices is equal to the sum of the shape vector elements.

In addition, it is crucial to establish the definition of the submatrices. The size of each submatrix can be determined using the shape vector, as it corresponds to the maximum number of polynomial terms that can be derived for a given harmonic number, based on the constraint $Q + 1$.

Moreover, a few observations can be made about the polynomial and harmonic parameters in the $[\tilde{L}_{jn}^{rm}]^{c,s}$ matrix:

- In each row of the matrix, the parameters m and n remain constant.
- In each column of the matrix, the parameters r and j are constant.
- Within a given submatrix, both m and r are constant.
- For a given submatrix, j and n vary according to the maximum number of polynomial terms that can be derived for the corresponding harmonic number, under the constraint $Q + 1$.

Based on these observations, helper vectors that will be used specifically for this algorithm are introduced to represent the pattern that the parameters m and n follow in the columns. These vectors will be referred to as \mathbf{v}_{2nd_arg} and \mathbf{v}_{4th_arg} , which correspond to the column indices for the m and n values, respectively.

To derive these vectors, two simple loops are used:

1. **Outer loop:** This loop iterates over $0 \leq m < M$. Before entering the inner loop, n is set to $m + 1$.
2. **Inner loop:** This loop iterates through the m -th element of the vector $\mathbf{v}_{\text{shape},c}$. For each distinct value of m , the inner loop runs a number of times as specified by the corresponding element of the shape vector. For example, if $m = 0$ and $M = Q = 3$, the inner loop will run twice.

The resulting vectors would be:

$$\mathbf{v}_{2nd_arg} = [0 \ 0 \ 1 \ 1 \ 2 \ 3]^T$$

$$\mathbf{v}_{4th_arg} = [1 \ 3 \ 2 \ 4 \ 3 \ 4]^T$$

The algorithm then proceeds by looping through the columns of the influence matrix. In each column, the loop iterates over $0 \leq r < M$. Before starting the inner loop, the polynomial

number is set $j = r + 1$. The inner loop then iterates through the r -th element of the $\mathbf{v}_{\text{shape},c}$ vector.

Within the inner loop, elements $[\tilde{L}_{jn}^{rm}]$ can be calculated using Eqn.18. The values for r and j are defined in the outer loop, while m and n are assigned the elements of v_{2nd_arg} and \mathbf{v}_{4th_arg} , respectively, using a counter that tracks the number of inner loop iterations. The maximum counter value should match the number of rows (or columns) in the influence matrix. Lastly, inside the inner loop, j is incremented by 2 after each iteration, and the row index is also incremented by 1.

It is important to note that the calculation of $[\tilde{L}_{jn}^{rm}]$ for the cosine and sine terms is different, and this is taken into account using a switch case.

The final inflow then can be easily calculated using Eq. 17.

The algorithm described in this section is visualized in Figure 3.

4.4 Loading Coefficients $[\tau_n^m]^{c,s}$ Calculation Algorithm

First, the previously derived loading coefficients and influence matrices will be used to calculate the induced velocity coefficients α_j^r and β_j^r according to Eq. 31.

The algorithm begins by looping through each azimuthal position. For each blade position, a nested loop iterates over the radial positions. Similarly to the calculation of the loading coefficients, the algorithm then runs over $0 \leq r < M$. Before the inner loop starts, the polynomial number j is set to $r + 1$. The inner loop then iterates through the r -th element of the $\mathbf{v}_{\text{shape},c}$ vector. Inside these loops, the inflow distribution is calculated using Eq.30.

The algorithm described in this section is visualized in Figure 4.

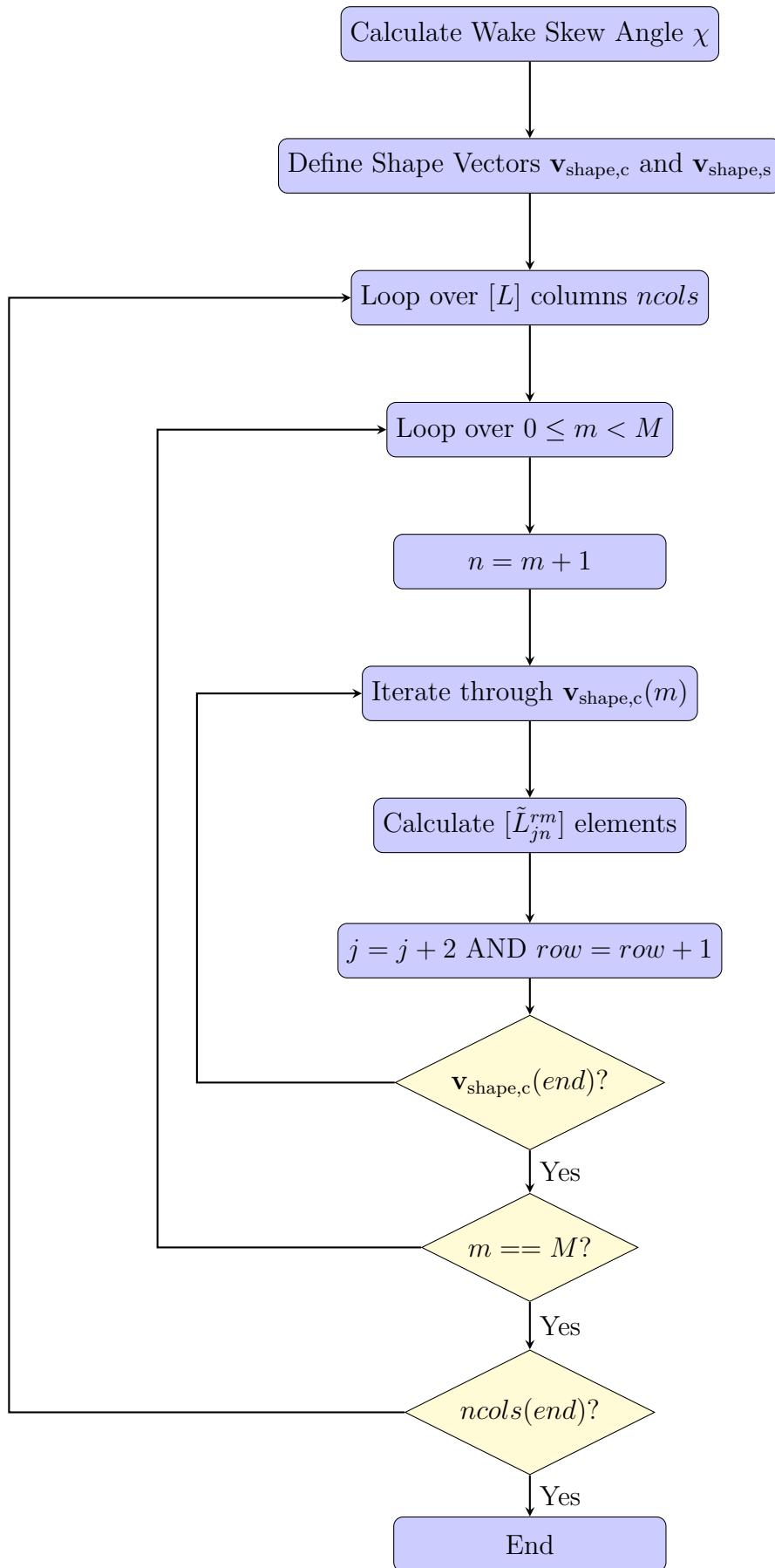


Figure 3: Influence Matrices $[\tilde{L}_{jn}^{rm}]^{c,s}$ Calculation Algorithm

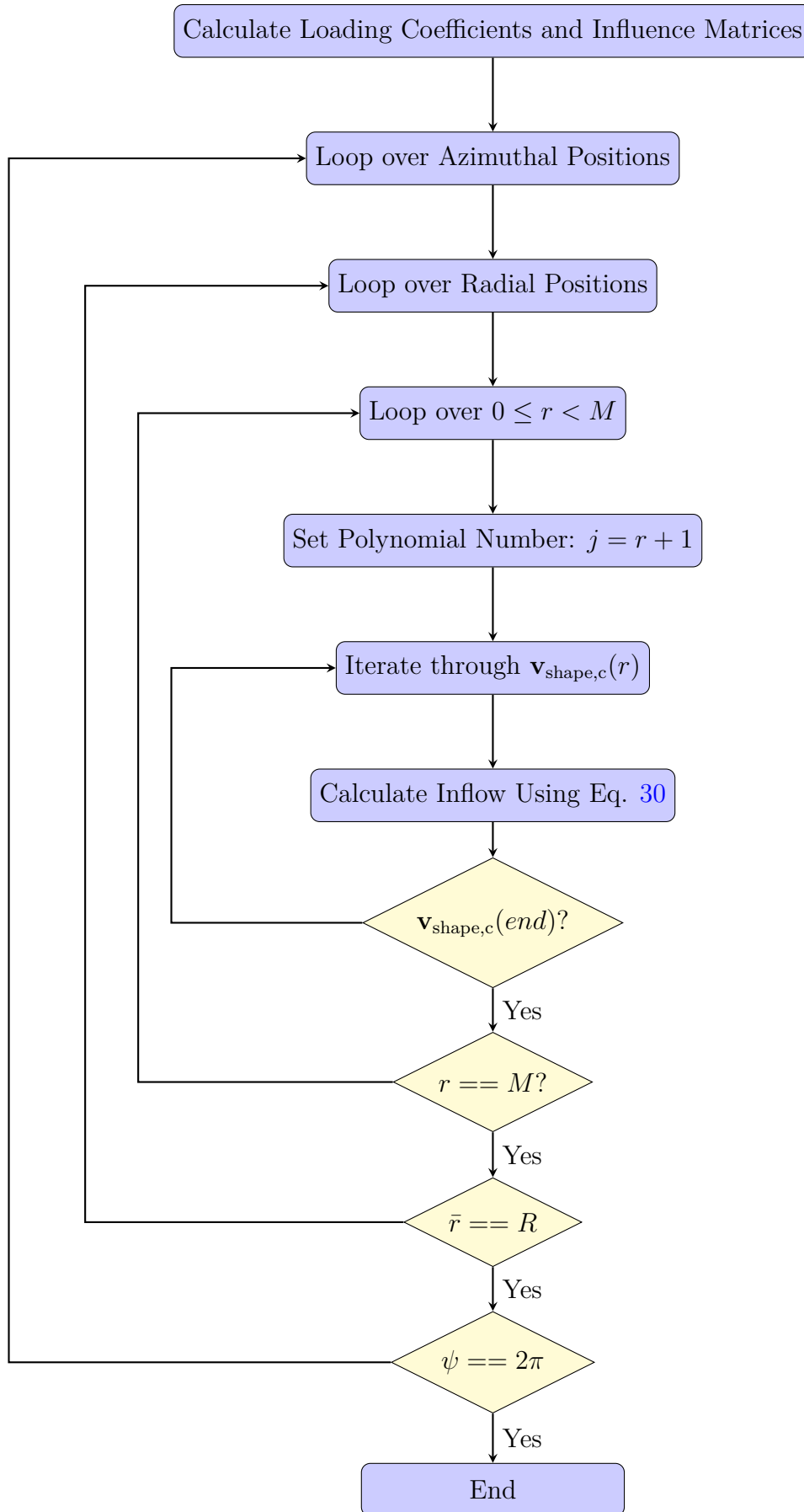


Figure 4: Inflow Distribution $w(\bar{r}, \psi)$ Calculation Algorithm

5 Results

5.1 BO-105 helicopter model description

This section contains the model description of the BO-105 helicopter.

Variable Name	Notation	Value	Units
Rotor radius	R	2	m
Number of blades	N_q	4	-
Rotor rotational speed	Ω	109.9557	rad/s
Blade sectional chord length	c	Table 7	m
Blade twist angle	θ_{tw}	Table 7	deg
Airfoil	-	Appendix A	-
Coning angle	β_0	2.5	deg

Table 5: BO-105 helicopter specifications

Table 5 provides the geometric specifications of the helicopter, while Table 6 outlines the operating conditions determined by the trimming process, along with external factors such as air density and speed of sound. There will be two cases examined for different advance ratios.

Variable Name	Notation	Value	Units
Advance ratio	μ	0.13 and 0.26	-
Shaft angle	a_{shaft}	-7.46	deg
Collective pitch angle	θ_0	6.5 and 8.5	deg
Longitudinal cyclic pitch angle	θ_{1c}	2.2 and 0.4	deg
Lateral cyclic pitch angle	θ_{1s}	-1.5 and -2.5	deg
Air density	ρ	1.202	kg/m^3
Speed of Sound	V_{sound}	347.219	m/s

Table 6: BO-105 helicopter operating conditions

The chord and twist angles are given as functions of the radial position of the blade section in Table 7.

5.2 Peters-He and Free Wake Lifting Line model results comparison

The BO-105 helicopter model, which was described in detail in the previous section, will be used to compare the rotor inflow distribution calculated using the Peters-He finite state inflow model with the distribution calculated using the free wake lifting line model [16].

The rotor is examined under two conditions with different advance ratios, $\mu = 0.13$ and $\mu = 0.26$.

The Peters-He simulation uses a polynomial and harmonic number of $M = Q = 3$, a design decision made to balance accuracy and computational efficiency. This combination was selected to accurately capture the inflow distribution without significantly increasing the compilation time, in hopes of making it suitable for real-time applications.

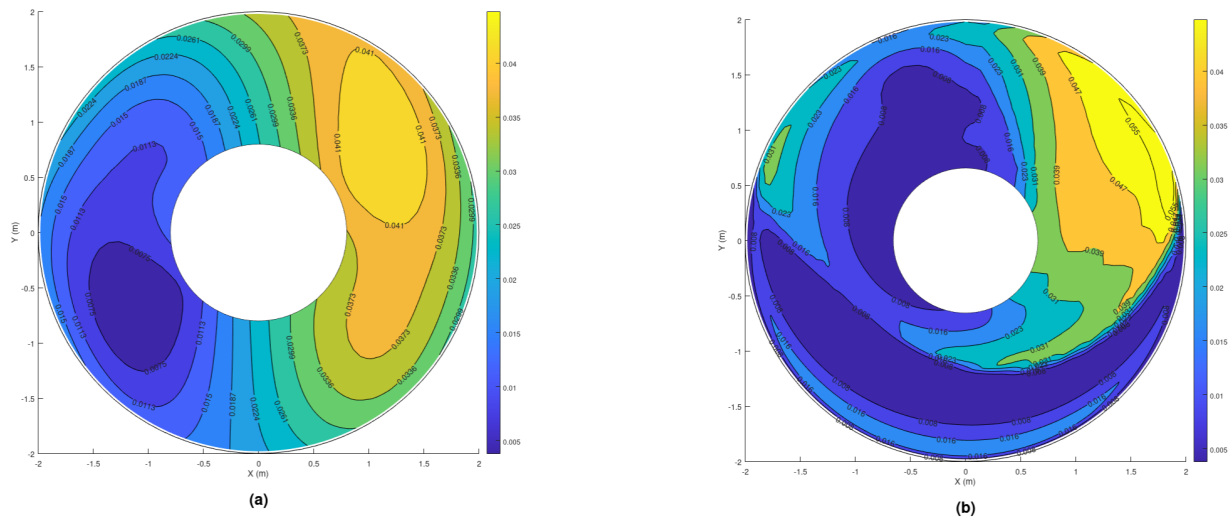
The variables used for the comparisons are:

Radius position r (m)	Chord c (m)	Twist angle θ_{tw} (deg)
0.250	0.121	-4.200
0.433	0.121	-4.200
0.497	0.121	-3.995
0.617	0.121	-3.535
0.745	0.121	-3.025
0.873	0.121	-2.515
1.000	0.121	-2.005
1.128	0.121	-1.495
1.256	0.121	-0.985
1.383	0.121	-0.475
1.511	0.121	0.035
1.639	0.121	0.545
1.767	0.121	1.055
2.000	0.121	2.000

Table 7: BO-105 helicopter blade chord and twist angle distribution as a function of radius

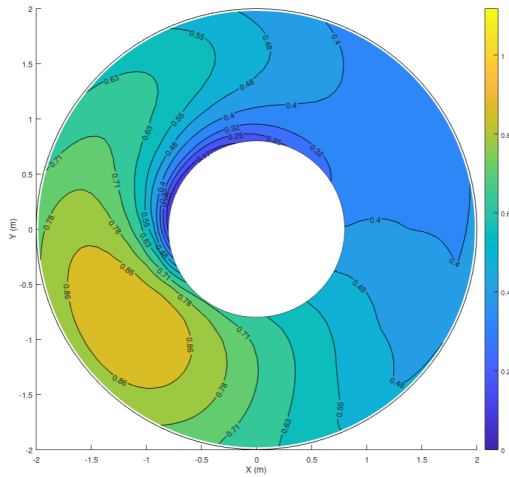
- The non-dimensional inflow, w_{inflow}
- Normal loading coefficient distribution, C_N
- Local blade element velocity distribution, U in m/s
- Angle of attack distribution, α in deg

Contour plots that illustrate the distributions of these variables across the rotor disc for an advance ratio of $\mu = 0.26$ are shown in Figures 15-15, while those for an advance ratio of $\mu = 0.13$ are shown in Figures 19-22.

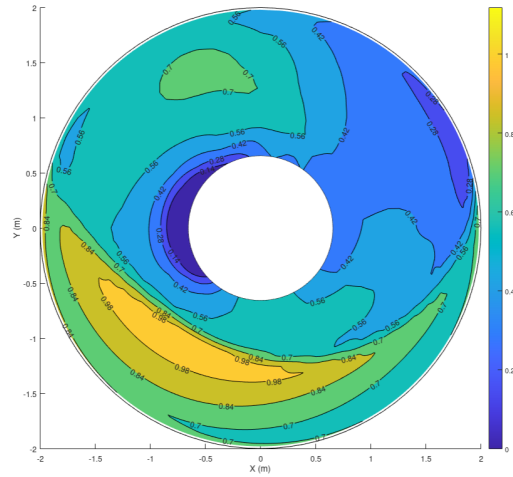
(a) Derived from Peters-He Theory for $M = 3$, $Q = 3$

(b) Derived from free wake lifting line model

Figure 5: BO-105: Inflow distribution w_{inflow} for $\mu = 0.26$



(a)

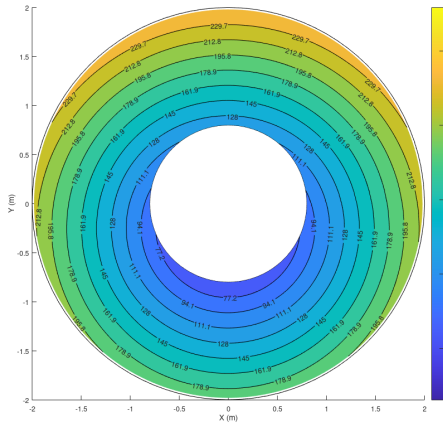


(b)

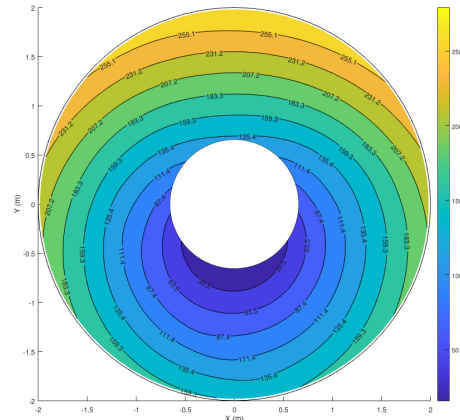
(a) Derived from Peters-He Theory for $M = 3$, $Q = 3$

(b) Derived from a free wake lifting line model

Figure 6: BO-105: Normal loading coefficient distribution C_N for $\mu = 0.26$



(a)



(b)

(a) Derived from Peters-He Theory for $M = 3$, $Q = 3$

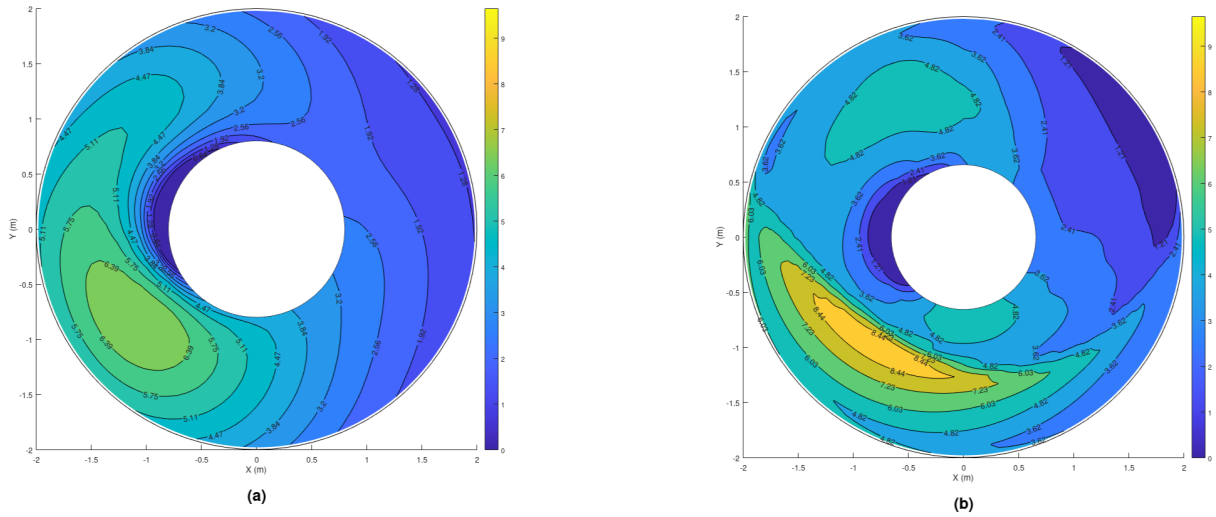
(b) Derived from a free wake lifting line model

Figure 7: BO-105: Local velocity distribution U for $\mu = 0.26$

In addition, plots for the same variables and advance ratios, as a function of the azimuth angle at $\bar{r} = 0.5$, are presented in Figures 23-24.

Some general observations can be made:

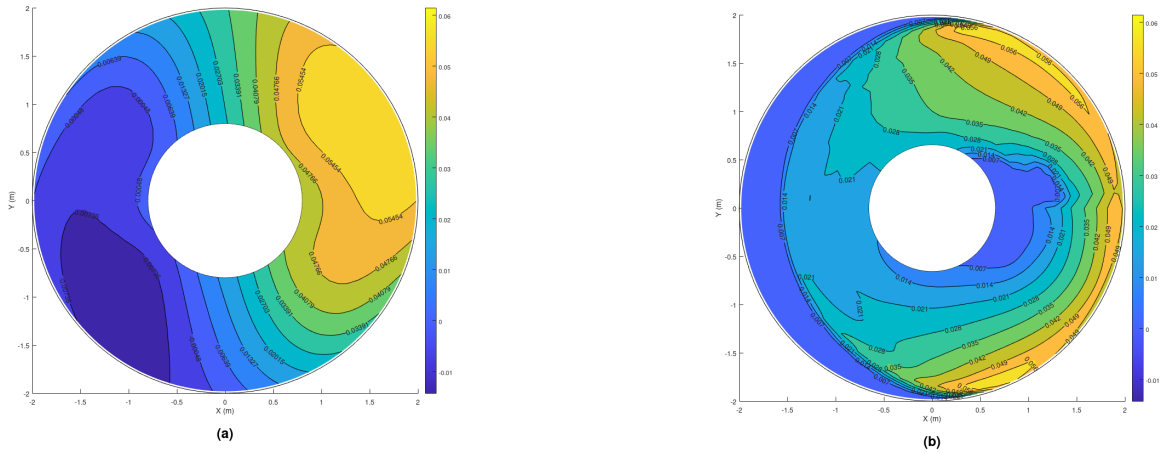
1. The wind velocity is aligned with the X-axis, pointing to the right.
2. The inflow plot shows that the front region, with the advancing side ($0^\circ \leq \psi \leq 180^\circ$) experiencing a greater inflow compared to the retreating side ($180^\circ \leq \psi \leq 360^\circ$).
3. As expected, the velocity is significantly higher on the advancing side and lower on the retreating side due to the rotation of the rotor.
4. As a result of the velocity difference, the angle of attack distribution plot shows that the advancing side of the rotor has a smaller angle of attack than the retreating side. To



(a) Derived from Peters-He Theory for $M = 3$, $Q = 3$

(b) Derived from a free wake lifting line model

Figure 8: BO-105: Angle of attack distribution α for $\mu = 0.26$



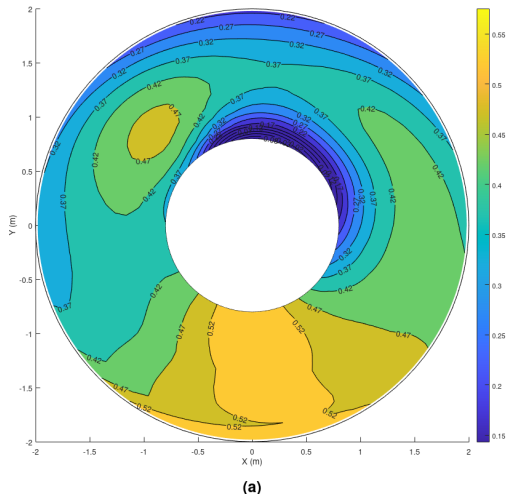
(a) Derived from Peters-He Theory for $M = 3$, $Q = 3$

(b) Derived from a free wake lifting line model

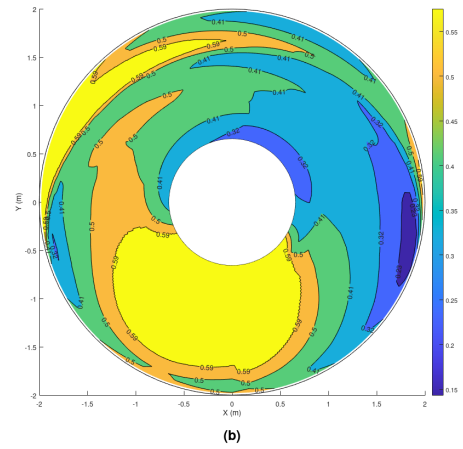
Figure 9: BO-105: Inflow distribution w_{inflow} for $\mu = 0.13$

compensate for this difference, the negative value of the longitudinal cyclic pitch angle θ_{1s} adjusts the pitch of the rotor blade. On the advancing side, the blade pitches downward, reducing the angle of attack, while on the retreating side, it pitches upward, increasing the angle of attack.

From the plots, one can conclude that the distributions, although not identical, follow a similar pattern. The free wake lifting line method offers higher fidelity and can model the inflow more accurately, but it is time-consuming and not suitable for real-time applications. Nevertheless, the distribution generated by the Peters-He simulation model, while not capturing all the phenomena, seems satisfactory for its intended purpose.

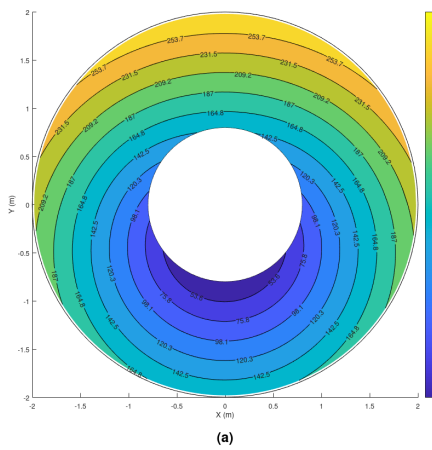


(a) Derived from Peters-He Theory for $M = 3$, $Q = 3$

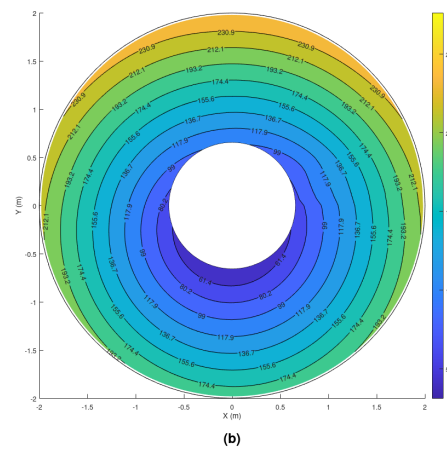


(b) Derived from a free wake lifting line model

Figure 10: BO-105: Normal loading coefficient distribution C_N for $\mu = 0.13$

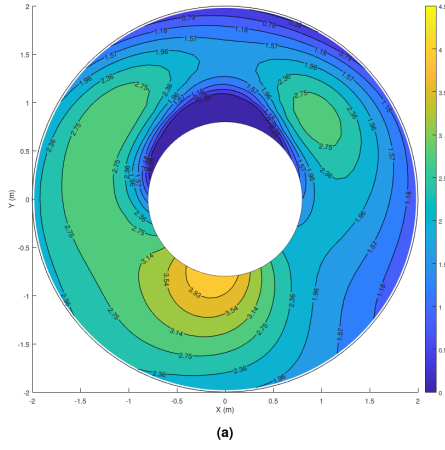


(a) Derived from Peters-He Theory for $M = 3$, $Q = 3$

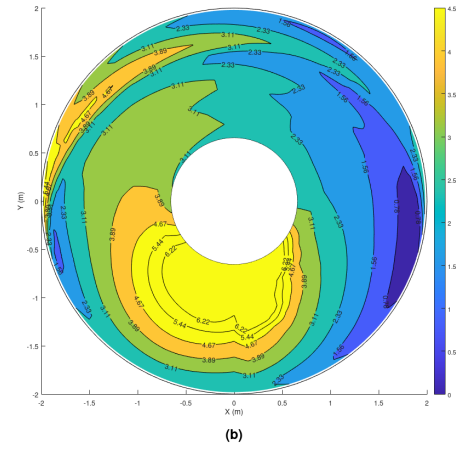


(b) Derived from a free wake lifting line model

Figure 11: BO-105: Local velocity distribution U for $\mu = 0.13$

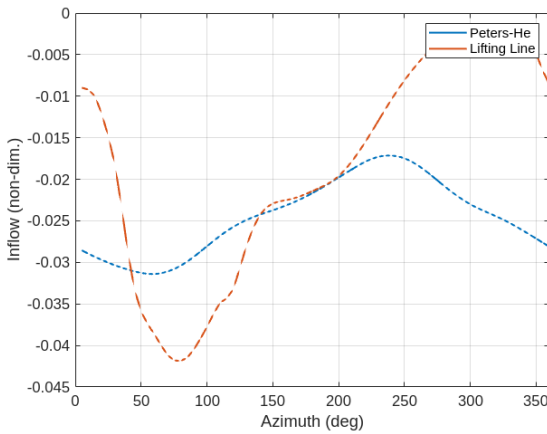


(a) Derived from Peters-He Theory for $M = 3$, $Q = 3$

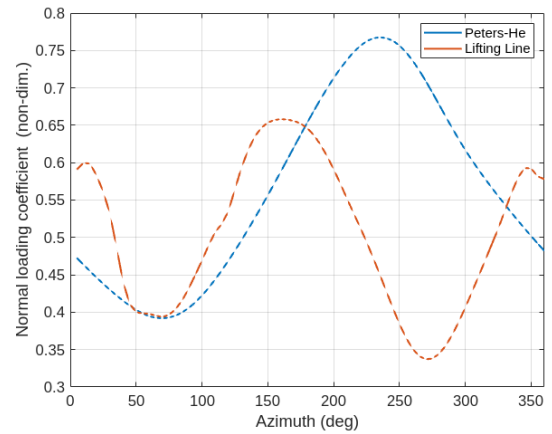


(b) Derived from a free wake lifting line model

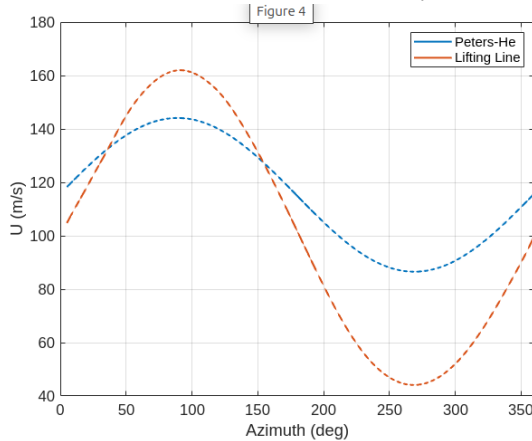
Figure 12: BO-105: Angle of attack distribution α for $\mu = 0.13$



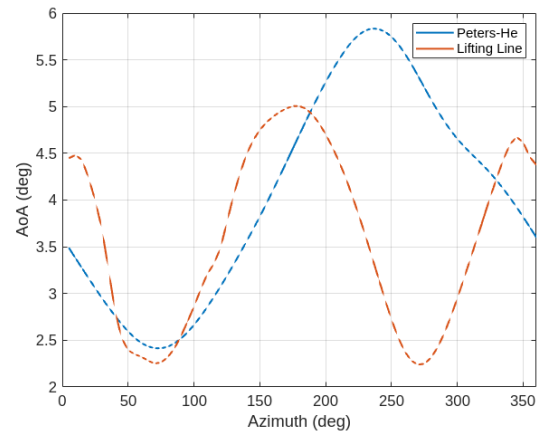
(a) Inflow distribution w_{inflow}



(b) Normal loading coefficient distribution C_N

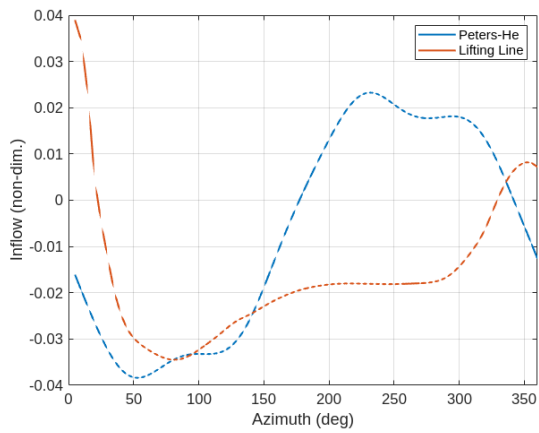


(c) Local velocity distribution U

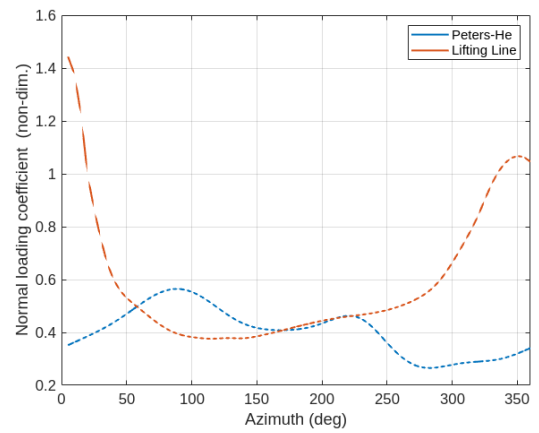


(d) Angle of attack distribution α

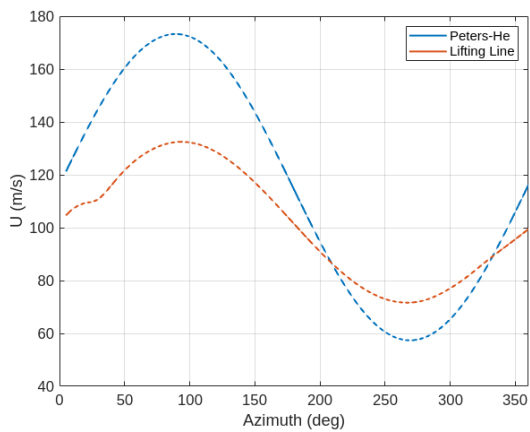
Figure 13: Results for $\mu = 0.26$ and $\bar{r} = 0.5$ as a function of azimuthal position



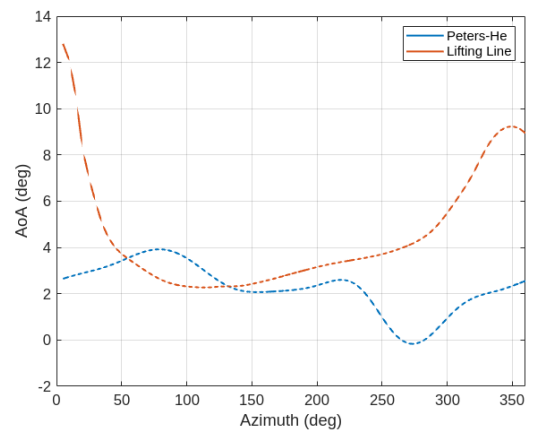
(a) Inflow distribution w_{inflow}



(b) Normal loading coefficient distribution C_N



(c) Local velocity distribution U



(d) Angle of attack distribution α

Figure 14: Results for $\mu = 0.13$ and $\bar{r} = 0.5$ as a function of azimuthal position

6 Conclusions

The primary objective of this thesis was to study the Peters-He finite-state inflow model, develop an open-source simulation code [14], and evaluate its potential for real-time applications, such as control systems. To assess the model's accuracy and computational efficiency, comparisons were made with a higher-fidelity model, the Free Wake Lifting Line Theory. The BO-105 helicopter model was used as a case study to examine the inflow distribution, the loading distribution, and the aerodynamic behavior under forward flight conditions.

The findings demonstrate that the Peters-He model offers advantages over simpler inflow models by incorporating higher harmonic responses and capturing more complex wake dynamics. However, the trade-off between computational cost and accuracy is evident. While the Peters-He model is computationally efficient and performs well in forward flight, it does not achieve the same level of accuracy as the Free Wake Lifting Line Theory, which offers greater fidelity but is far more resource-intensive.

Additionally, the model's assumptions of quasi-static conditions mean it may not fully capture the intricate details of highly dynamic flight maneuvers. Despite this, the Peters-He model remains suitable for practical applications, especially for real-time simulations, where a balance between speed and accuracy is required.

In conclusion, the open-source simulation code developed in this thesis demonstrates the potential of the Peters-He model for real-time rotorcraft aerodynamics simulations. Although further refinements may be needed in the future to handle more dynamic flight conditions and fast maneuvering, the model balances computational efficiency and sufficient accuracy, making it well-suited for a range of real-time applications.

Nomenclature

$[M]$	Apparent mass matrix
$[L]$	Influence matrix
α	Angle of attack, deg
α_{shaft}	Shaft angle of attack, deg
\bar{r}	Non-dimensional blade section radial location, r/R
β	Blade flapping angle, deg
β_0	Coning angle, deg
β_{1c}	Longitudinal cyclic flapping angle, deg
β_{1s}	Lateral cyclic flapping angle, deg
χ	Wake skew angle, deg
κ	Induced power factor
λ	Total inflow ratio, $\lambda_f + \lambda_m$
λ_0	Uniform inflow ratio
λ_c	Climb ratio, $V_c/\Omega R$
λ_f	Free-stream inflow ratio, $\frac{V_\infty \sin(\alpha_{shaft})}{\Omega R}$
λ_i	Inflow ratio
λ_m	Mean inflow in momentum expression
μ	Advance ratio
Ω	Rotational speed, rad/s
ϕ	Inflow angle, deg
ϕ_s	Shaft side tilt angle, deg
ϕ_j^r	Radial expansion function
ψ	Azimuth angle, deg
τ_n^m	Loading coefficients
θ	Blade pitch at radial position \bar{r}
θ_0	Collective pitch angle, deg
θ_{0-75}	Blade collective pitch angle at $\bar{r} = 0.75$, deg

θ_{1c}	Longitudinal cyclic pitch angle, deg
θ_{1s}	Lateral cyclic pitch angle, deg
θ_{tw}	Blade twist (root-tip), deg
c	Blade sectional chord length, m
c_D	Sectional drag coefficient
c_L	Sectional lift coefficient
dF_x	Sectional tangential force, N
dF_z	Rotor normal force on a section, N
dr	Blade sectional span, m
H_j^r	Factorial combination
i	Blade section index
j, n	Polynomial number (shape function index)
K_c	Ratio of cosine component to mean value of the first harmonic inflow
K_s	Ratio of sine component to mean value of the first harmonic inflow
L_i^q	Lift on the q -th blade i -th section, N
L_{jn}^{rm}	Elements in the $[L]$ matrix
N_i	Number of sections per blade
N_q	Number of blades
Q	Highest power of \bar{r}
q	Blade index
r, m	Harmonic number
R	Rotor radius, m
r	Blade section radial position, m
U	Blade sectional free-stream velocity, m/s
U_P	Blade sectional perpendicular velocity, m/s
U_T	Blade sectional tangential velocity, m/s
V_∞	Forward speed, m/s
$w(\bar{r}, \psi)$	Inflow ratio, $V_i/\Omega R$

A Appendix: BO-105 helicopter polar data

AoA (deg)	Mach 0.00			Mach 0.20			Mach 0.40		
	C_L	C_D	C_M	C_L	C_D	C_M	C_L	C_D	C_M
-20	-0.7495	0.3272	0.0900	-0.7495	0.3272	0.0900	-0.7495	0.3272	0.0900
-14	-1.1167	0.0264	0.0010	-1.1167	0.0264	0.0010	-0.9000	0.0200	0.0600
-11	-1.0500	0.0149	0.0005	-1.0500	0.0149	0.0005	-0.8600	0.0120	0.0230
-9	-0.8433	0.0120	-0.0013	-0.8433	0.0120	-0.0013	-0.7500	0.0115	-0.0150
-7	-0.6300	0.0092	-0.0040	-0.6300	0.0092	-0.0040	-0.5800	0.0115	-0.0100
-4	-0.2845	0.0081	-0.0071	-0.2845	0.0081	-0.0071	-0.3316	0.0113	-0.0069
-2	-0.0717	0.0080	-0.0079	-0.0717	0.0080	-0.0079	-0.1030	0.0104	-0.0073
0	0.1230	0.0062	-0.0077	0.1230	0.0062	-0.0077	0.1256	0.0106	-0.0077
2	0.3338	0.0067	-0.0077	0.3338	0.0067	-0.0077	0.3542	0.0105	-0.0087
4	0.5446	0.0072	-0.0077	0.5446	0.0072	-0.0077	0.5828	0.0108	-0.0099
6	0.7590	0.0083	-0.0078	0.7590	0.0083	-0.0078	0.8114	0.0120	-0.0092
8	0.9770	0.0102	-0.0079	0.9770	0.0102	-0.0079	1.0400	0.0133	-0.0076
9	1.0860	0.0112	-0.0079	1.0860	0.0112	-0.0079	1.1543	0.0137	-0.0058
10	1.1950	0.0121	-0.0080	1.1950	0.0121	-0.0080	1.2500	0.0153	-0.0034
11	1.2875	0.0141	-0.0002	1.2875	0.0141	-0.0079	1.3500	0.0175	0.0010
12	1.3800	0.0160	0.0077	1.3800	0.0160	-0.0077	1.4250	0.0205	0.0041
13	1.4200	0.0180	0.0077	1.4200	0.0180	-0.0077	1.3950	0.0283	-0.0052
14	1.5000	0.0210	-0.0077	1.5000	0.0210	-0.0077	1.1400	0.1183	-0.0565
15	1.5500	0.0315	-0.0600	1.5500	0.0316	-0.0600	1.0300	0.2250	-0.1080
16	1.5132	0.0663	-0.0937	1.5132	0.0664	-0.0937	1.2000	0.3400	-0.1100
20	0.7497	0.3272	-0.0900	0.7497	0.3272	-0.0900	0.7496	0.3272	-0.0900

Table 8: Aerodynamic Coefficients C_L , C_D , and C_M for Mach 0.00, 0.20, and 0.40

AoA (deg)	Mach 0.50			Mach 0.60			Mach 0.70		
	C_L	C_D	C_M	C_L	C_D	C_M	C_L	C_D	C_M
-20	-0.7495	0.3272	0.0900	-0.7495	0.3272	0.0900	-0.7495	0.3272	0.0900
-14	-0.8560	0.0948	0.0448	-0.8000	0.2450	0.0500	-0.7724	0.2806	0.0525
-11	-0.9040	0.0342	0.0142	-0.8225	0.1077	0.0230	-0.7840	0.2260	0.0300
-9	-0.8800	0.0133	-0.0110	-0.8350	0.0460	0.0035	-0.7920	0.1480	0.0100
-7	-0.7450	0.0240	-0.0130	-0.8000	0.0700	-0.0100	-0.7067	0.0953	0.0013
-4	-0.3600	0.0141	-0.0105	-0.4160	0.0181	-0.0188	-0.4980	0.0268	-0.0181
-2	-0.1060	0.0104	-0.0071	-0.1030	0.0106	-0.0073	-0.1226	0.0107	-0.0120
0	0.1376	0.0103	-0.0084	0.1540	0.0101	-0.0089	0.1708	0.0102	-0.0093
2	0.3812	0.0104	-0.0092	0.4110	0.0106	-0.0093	0.4642	0.0186	-0.0076
4	0.6248	0.0111	-0.0094	0.6680	0.0131	-0.0057	0.6700	0.0483	-0.0224
6	0.8684	0.0125	-0.0075	0.9050	0.0292	0.0000	0.7700	0.1000	-0.0508
8	1.1120	0.0153	-0.0003	0.9900	0.0662	-0.0107	0.8900	0.1730	-0.0650
9	1.2000	0.0210	0.0056	1.0200	0.0920	-0.0231	0.9000	0.2200	-0.0700
10	1.2700	0.0300	0.0124	1.0680	0.1300	-0.0315	0.8900	0.2590	-0.0735
11	1.2900	0.0482	0.0140	1.0690	0.1875	-0.0383	0.8800	0.2980	-0.0770
12	1.2100	0.0850	0.0037	1.0700	0.2450	-0.0450	0.8667	0.3387	-0.0790
13	1.1800	0.1650	-0.0186	1.0200	0.2983	-0.0513	0.8533	0.3793	-0.0810
14	1.1500	0.2450	-0.0438	0.9700	0.3517	-0.0577	0.8400	0.4200	-0.0830
15	1.1350	0.2925	-0.0719	0.9200	0.4050	-0.0640	0.8249	0.4045	-0.0842
16	1.1200	0.3400	-0.1000	0.8859	0.3894	-0.0692	0.8098	0.3891	-0.0853
20	0.7496	0.3272	-0.0900	0.7495	0.3272	-0.0900	0.7495	0.3272	-0.0900

Table 9: Aerodynamic Coefficients C_L , C_D , and C_M for Mach 0.50, 0.60, and 0.70

AoA (deg)	Mach 0.80			Mach 0.85			Mach 0.90		
	C_L	C_D	C_M	C_L	C_D	C_M	C_L	C_D	C_M
-20	-0.7495	0.3272	0.0900	-0.7495	0.3272	0.0900	-0.7495	0.3272	0.0900
-14	-0.7724	0.2806	0.0525	-0.7500	0.2520	0.0680	-0.7274	0.2521	0.0765
-11	-0.7840	0.2260	0.0300	-0.7500	0.1850	0.0390	-0.7125	0.2058	0.0673
-9	-0.7920	0.1480	0.0100	-0.7500	0.1403	0.0197	-0.6975	0.1633	0.0578
-7	-0.7067	0.0953	0.0013	-0.6550	0.1225	0.0465	-0.6075	0.1980	0.0448
-4	-0.4980	0.0268	-0.0181	-0.4760	0.0580	0.0242	-0.2820	0.0700	0.0088
-2	-0.1226	0.0107	-0.0120	-0.1180	0.0110	-0.0096	-0.1600	0.0138	-0.0142
0	0.1708	0.0102	-0.0093	0.1840	0.0132	-0.0082	0.2290	0.0287	-0.0330
2	0.4642	0.0186	-0.0076	0.4860	0.0383	-0.0253	0.3500	0.0660	-0.0514
4	0.6700	0.0483	-0.0224	0.5650	0.0741	-0.0523	0.4500	0.1000	-0.0579
6	0.7700	0.1000	-0.0508	0.6600	0.1118	-0.0669	0.5400	0.1370	-0.0720
8	0.8900	0.1730	-0.0650	0.7500	0.1520	-0.0730	0.6000	0.1760	-0.0800
9	0.9000	0.2200	-0.0700	0.7500	0.1712	-0.0752	0.6217	0.1973	-0.0815
10	0.8900	0.2590	-0.0735	0.7500	0.1903	-0.0773	0.6433	0.2187	-0.0830
11	0.8800	0.2980	-0.0770	0.7500	0.2095	-0.0795	0.6650	0.2400	-0.0845
12	0.8667	0.3387	-0.0790	0.7500	0.2287	-0.0817	0.6867	0.2613	-0.0860
13	0.8533	0.3793	-0.0810	0.7500	0.2478	-0.0838	0.7083	0.2827	-0.0875
14	0.8400	0.4200	-0.0830	0.7500	0.2670	-0.0860	0.7300	0.3040	-0.0890
15	0.8249	0.4045	-0.0842	0.7499	0.2770	-0.0867	0.7332	0.3079	-0.0892
16	0.8098	0.3891	-0.0853	0.7498	0.2871	-0.0873	0.7365	0.3117	-0.0893
20	0.7495	0.3272	-0.0900	0.7495	0.3272	-0.0900	0.7495	0.3272	-0.0900

Table 10: Aerodynamic Coefficients C_L , C_D , and C_M for Mach 0.80, 0.85, and 0.90

References

- [1] P. J. Carpenter and B. Fridovich. *Effect of a Rapid-Pitch Response of the Thrust and Induced-Velocity Response of a Full-Scale Helicopter Rotor*. Tech. rep. TN 3044. NACA, 1953.
- [2] Robert T. N. Chen. “A survey of nonuniform inflow models for rotorcraft flight dynamics and control applications”. In: 1990. URL: <https://api.semanticscholar.org/CorpusID:73583501>.
- [3] Robert P. Coleman, Arnold M. Feingold, and Carl W. Stempin. “Evaluation of the Induced-Velocity Field of an Idealized Helicopter Rotor”. In: 1945. URL: <https://api.semanticscholar.org/CorpusID:118625894>.
- [4] H. C. Jr. Curtiss and N. K. Shupe. “Stability and Control Theory for Hingeless Rotors”. In: *Proceedings of the Annual Forum of the American Helicopter Society*. May 1971.
- [5] Cheng Jian He David A. Peters David Doug Boyd. “Finite-State Induced-Flow Model for Rotors in Hover and Forward Flight”. In: *Journal of the American Helicopter Society* 34(5) (1989), pp. 5–17.
- [6] J Meijer Drees. “A theory of airflow through rotors and its application to some helicopter problems”. In: *Ann. Forum AHS* (1979). URL: <https://api.semanticscholar.org/CorpusID:264571735>.
- [7] J. Elliott and S. Althoff. *Inflow Measurement Made with a Laser Velocimeter on a Helicopter Model in Forward Flight*. Tech. rep. 100541-100545. NASA Technical Report, 1988.
- [8] H. Glauert and Aeronautical Research Committee. *A General Theory of the Autogyro*. Aeronautical Research Committee reports and memoranda. His Majesty Stationery Office, 1926. URL: <https://books.google.gr/books?id=8jIPnQEACAAJ>.
- [9] Hermann Glauert. “An aerodynamic theory of the airscrew”. In: URL: <https://api.semanticscholar.org/CorpusID:117983916>.
- [10] Feyyaz Güner. “Comparison of rotor inflow models for flight simulation fidelity”. PhD thesis. Sept. 2016.
- [11] James John Howlett. “UH-60A Black Hawk engineering simulation program. Volume 1: Mathematical model”. In: 1981. URL: <https://api.semanticscholar.org/CorpusID:107003905>.
- [12] Ioannis Karatsivoulis. “Helicopter flight dynamic modelling with state-of-the-art Dynamic Inflow”. PhD thesis. June 2020. DOI: [10.13140/RG.2.2.33321.83049](https://doi.org/10.13140/RG.2.2.33321.83049).
- [13] Sicheng Kevin Li. “Development of Rotorcraft Forward Flight Analysis Code Using the Finite-State Dynamic Inflow Model”. PhD thesis. Aug. 2020. DOI: [10.13140/RG.2.2.31206.86082](https://doi.org/10.13140/RG.2.2.31206.86082).
- [14] Victoria Malyshkina. *Peters-He inflow model*. https://gitlab.com/victoria_malyshkina/peters-he-inflow-model. Accessed: 2024-10-07.
- [15] Robert Niemiec and Farhan Gandhi. “Effects of Inflow Model on Simulated Aeromechanics of a Quadrotor Helicopter”. In: May 2016.

-
- [16] F. Nitzsche et al. “A new comprehensive analysis tool for the preliminary design and design evaluation of helicopters – the CORAL project”. In: *47th European Rotorcraft Forum*. Online, 2021.
- [17] R. A. Ormiston and D. A. Peters. “Hingeless Helicopter Rotor Response with Nonuniform Inflow and Elastic Blade Bending”. In: *Journal of Aircraft* 9.10 (Oct. 1972), pp. 690–696.
- [18] P. R. Payne. *Helicopter Dynamics and Aerodynamics*. Sir Isaac Pitman and Sons, LTD., 1959.
- [19] D. Peters and C. He. “Correlation of Measured Induced Velocities with a Finite-State Wake Model”. In: *Journal of the American Helicopter Society* 36.3 (1991), pp. 59–70.
- [20] D. A. Peters. “Hingeless Rotor Frequency Response with Unsteady Inflow”. In: *NASA SP-362*. Feb. 1974.
- [21] Dale Pitt and David Peters. “Theoretical prediction of dynamic-inflow derivatives”. In: *Vertica* 5 (Jan. 1981).
- [22] John B. Wheatley. “An aerodynamic analysis of the autogiro rotor with a comparison between calculated and experimental results”. In: 1935. URL: <https://api.semanticscholar.org/CorpusID:108085263>.
- [23] F. White and B. B. Blake. “Improved Method of Predicting Helicopter Control Response and Gust Sensitivity”. In: *The Journal of the Helicopter Association of Great Britain* (1949).



ΕΘΝΙΚΟ ΜΕΤΣΟΒΙΟ ΠΟΛΥΤΕΧΝΕΙΟ
ΣΧΟΛΗ ΜΗΧΑΝΟΛΟΓΩΝ ΜΗΧΑΝΙΚΩΝ
ΤΟΜΕΑΣ ΡΕΥΣΤΩΝ

ΔΙΠΛΩΜΑΤΙΚΗ ΕΡΓΑΣΙΑ

ΕΚΤΕΝΗΣ ΠΕΡΙΛΗΨΗ ΣΤΑ ΕΛΛΗΝΙΚΑ

ΑΕΡΟΔΥΝΑΜΙΚΗ ΑΝΑΛΥΣΗ ΔΡΟΜΕΑ
ΕΛΙΚΟΠΤΕΡΟΥ ΣΕ ΟΡΙΖΟΝΤΙΑ ΠΤΗΣΗ ΜΕ
ΧΡΗΣΗ ΤΟΥ ΜΟΝΤΕΛΟΥ PETERS-HE

Συγγραφέας:
ΒΙΚΤΩΡΙΑ ΜΑΛΙΣΚΙΝΑ

Επιβλέπων καθηγητής:
ΒΑΣΙΛΕΙΟΣ ΡΙΖΙΩΤΗΣ

ΑΘΗΝΑ,
14 ΟΚΤΩΒΡΙΟΥ 2024

Η παρούσα διπλωματική εργασία επικεντρώνεται στην αεροδυναμική ανάλυση της δυναμικής πτήσης των ελικοπτέρων χρησιμοποιώντας το μοντέλο αεροδυναμικής επαγωγής πεπερασμένων καταστάσεων Peters-He.

Η χρήση ενός μοντέλου που αποδίδει με επαρκή ακρίβεια την ανομοιόμορφη κατανομή των επαγομένων ταχυτήτων σε έναν δρομέα ελικοπτέρου είναι ζωτικής σημασίας για την ορθή μοντελοποίηση της εμπρόσθιας πτήσης, καθώς η παραδοχή ότι η ροή είναι αξονοσυμμετρική οδηγεί σε σημαντικά σφάλματα στους υπολογισμούς.

Τα διαθέσιμα υπολογιστικά μοντέλα, όπως η υπολογιστική ρευστοδυναμική (CFD) και οι μέθοδοι συνοριακών στοιχείων (panel methods), είναι εξαιρετικά υπολογιστικά απαιτητικά, γεγονός που τα καθιστά ακατάλληλα για εφαρμογές σε πραγματικό χρόνο. Αντίθετα, η χρήση ενός μοντέλου πεπερασμένων καταστάσεων για τον υπολογισμό της επαγομένης ροής δύναται να παρέχει μια ισορροπημένη λύση, αποτυπώνοντας με επαρκή ακρίβεια την κατανομή της ροής, ενώ παράλληλα απαιτεί σαφώς μικρότερο υπολογιστικό κόστος. Ένα τέτοιο μοντέλο θα μπορούσε να είναι κατάλληλο για εφαρμογές σε πραγματικό χρόνο, όπως είναι οι προσομοιώσεις της δυναμικής πτήσης και η αξιολόγηση των συστημάτων ελέγχου.

Ο στόχος της διπλωματικής εργασίας είναι η δημιουργία ενός γρήγορου και ευέλικτου εργαλείου, το οποίο χρησιμοποιεί το μοντέλο αεροδυναμικής επαγωγής πεπερασμένων καταστάσεων Peters-He σε συνδυασμό με τη θεωρία Blade Element για την ανάλυση της απόδοσης ελικοπτέρων τόσο σε εμπρόσθια πτήση όσο και σε αιώρηση.

Η απόδοση αυτού του μοντέλου θα συγκριθεί με ένα μοντέλο γραμμής άνωσης ελεύθερου ομόρρου, το οποίο προσφέρει υψηλότερη ακρίβεια αλλά είναι υπολογιστικά απαιτητικό και ακατάλληλο για εφαρμογές που απαιτούν υπολογισμούς σε πραγματικό χρόνο.

Με την αύξηση των βαθμών ελευθερίας στο μοντέλο Peters-He, είναι δυνατό να παρατηρήσει κανείς ότι δύναται να επιτευχθούν αποτελέσματα παρόμοια με αυτά του μοντέλου γραμμής άνωσης ελεύθερου ομόρρου, αλλά με σημαντικά μειωμένες υπολογιστικές απαιτήσεις. Οι μειωμένες χρονικές απαιτήσεις δύναται να καταστήσουν τον κώδικα κατάλληλο για εφαρμογές σε πραγματικό χρόνο.

Αν και παρόμοια υπολογιστικά μοντέλα έχουν αναπτυχθεί, δεν είναι διαθέσιμα στη γενική επιστημονική κοινότητα. Για την αντιμετώπιση αυτού του σημαντικού κενού, οι προσομοιώσεις που αναπτύχθηκαν για αυτήν τη διπλωματική εργασία είναι ανοιχτού κώδικα, με την πρόθεση να ωφεληθεί την ευρύτερη ακαδημαϊκή κοινότητα.

Το δυναμικό μοντέλο πεπερασμένων καταστάσεων ομόρρου Peters-He εφαρμόζει τη διακριτοποίηση των πτερυγίων, όπου η επαγόμενη ροή για κάθε τμήμα υπολογίζεται μέσω επαναληπτικής διαδικασίας. Παράλληλα, εισάγονται πολλαπλοί βαθμοί ελευθερίας ή καταστάσεις επαγόμενης ροής, οι οποίοι συνδυάζονται στο τέλος για τον υπολογισμό της τελικής κατανομής της ροής. Καθώς αυξάνονται οι βαθμοί ελευθερίας, βελτιώνεται και η ακρίβεια του υπολογισμού της κατανομής της επαγόμενης ροής. Αυτές οι καταστάσεις εκφράζονται αξιμουθιακά μέσω σειρών Fourier και ακτινικά μέσω συναρτήσεων Legendre.

Συγκεκριμένα, η κατανομή των επαγόμενων ταχυτήτων ως συνάρτηση της αξιμουθιακής και ακτινικής θέσης περιγράφεται από την εξίσωση 30. Υιοθετείται η παραδοχή ότι το πεδίο των ταχυτήτων είναι ανεξάρτητο του χρόνου.

$$w(\bar{r}, \psi) = \sum_{r=0}^{\infty} \sum_{j=r+1, r+3, \dots}^{\infty} \phi_j^r(\bar{r}) [\alpha_j^r \cos(r\psi) + \beta_j^r \sin(r\psi)] \quad (30)$$

Η εξίσωση 30 υποδεικνύει ότι η επαγόμενη ροή δύναται να αναπαρασταθεί μέσω των συντελεστών επαγόμενης ροής $\{\alpha_j^r\}$ και $\{\beta_j^r\}$, οι οποίοι εμφανίζονται σε διανυσματική μορφή.

Οι συντελεστές επαγόμενης ροής μπορούν να υπολογιστούν χρησιμοποιώντας τις εξισώσεις 31. Αυτές οι εξισώσεις συσχετίζουν τους συντελεστές επαγόμενης ροής με τους συντελεστές

φόρτισης του ρότορα $\{\tau_m^n\}^{c,s}$ μέσω των σταθερών πινάκων $[L_{jn}^{rm}]^{c,s}$, οι οποίοι εξαρτώνται από τις συνθήκες πτήσης.

$$\begin{aligned} \begin{bmatrix} \vdots \\ \{\alpha_j^r\} \\ \vdots \end{bmatrix} &= [L_{jn}^{rm}]^c \begin{bmatrix} \vdots \\ \{\tau_m^n\}^c \\ \vdots \end{bmatrix} \\ \begin{bmatrix} \vdots \\ \{\beta_j^r\} \\ \vdots \end{bmatrix} &= [L_{jn}^{rm}]^s \begin{bmatrix} \vdots \\ \{\tau_m^n\}^s \\ \vdots \end{bmatrix} \end{aligned} \quad (31)$$

Για την ανάπτυξη του κώδικα χρησιμοποιήθηκε η τεχνική του αντικειμενοστρεφή προγραμματισμού (Object-Oriented Programming). Αυτή η τεχνική επιλέχθηκε με στόχο τη βελτίωση της οργάνωσης και της επαναχρησιμοποίησης του κώδικα. Με την ενσωμάτωση συναφών μεταβλητών και μεθόδων σε κλάσεις, ο κώδικας καθίσταται πιο δομημένος και εύκολος στη διαχείριση. Αυτή η προσέγγιση επιτρέπει επίσης την επαναχρησιμοποίηση κοινών λειτουργιών και καθιστά πιο εύκολη την επέκταση της προσομοίωσης με την προσθήκη νέων μεθόδων στο μέλλον.

Τέλος, γίνεται σύγκριση των αποτελεσμάτων της προσομοίωσης χρησιμοποιώντας το μοντέλο Peters-He με ένα υπάρχον μοντέλο γραμμής άνωσης ελεύθερου ομόρρου που έχει αναπτυχθεί στο Εργαστήριο Αεροδυναμικής του Εθνικού Μετσόβιου Πολυτεχνείου, χρησιμοποιώντας τα γεωμετρικά χαρακτηριστικά του ελικοπτέρου BO-105.

Εξετάζονται δυο περιπτώσεις με διαφορετικούς λόγους προώθησης, $\mu = 0.13$ και $\mu = 0.26$.

Η προσομοίωση με το μοντέλο Peters-He χρησιμοποιεί πολυωνυμικό και αρμονικό αριθμό $M = Q = 3$. Ο συνδυασμός των αριθμών αυτών ορίζουν τους βαθμούς ελευθερίας της προσομοίωσης.

Οι τιμές που επιλέχθηκαν αποτελούν μια σχεδιαστική απόφαση που πάρθηκε για να ισορροπήσει την ακρίβεια και την υπολογιστική πολυπλοκότητα. Ο συνδυασμός αυτός επιλέχθηκε ώστε να αποτυπώνει με ακρίβεια την κατανομή της επαγόμενης ροής χωρίς να αυξάνει σημαντικά τον χρόνο εκτέλεσης του προγράμματος, με στόχο την καταλληλότητα του μοντέλου για εφαρμογές σε πραγματικό χρόνο.

Οι μεταβλητές που χρησιμοποιούνται για τις συγκρίσεις είναι:

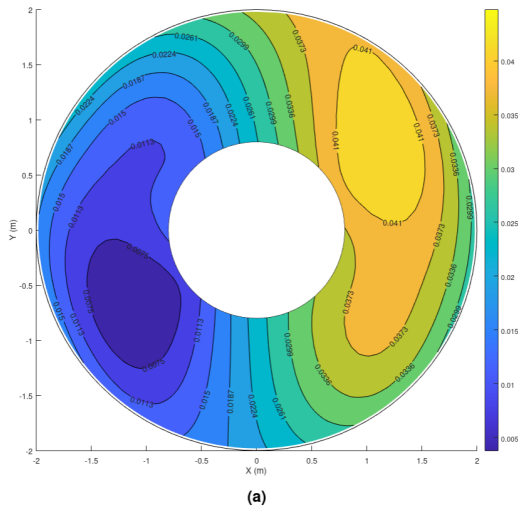
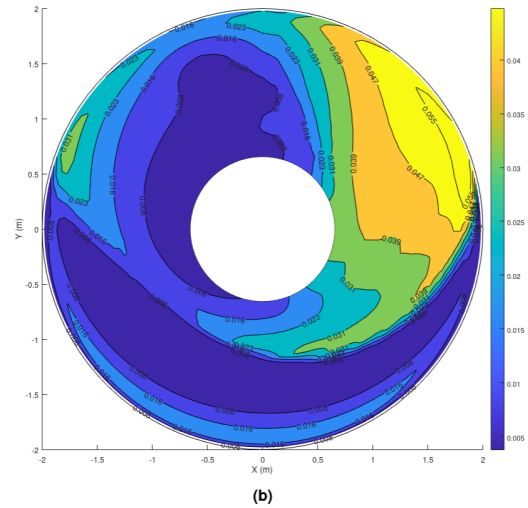
- Οι αδιάστατες επαγόμενες ταχύτητες, w_{inflow}
- Η κατανομή του συντελεστή κάθετης φόρτισης, C_N
- Η κατανομή της τοπικής ταχύτητας, U σε m/s
- Η κατανομή της γωνίας προσβολής, α σε deg

Τα διαγράμματα κατανομής αυτών των μεταβλητών στον δίσκο του δρομέα παρουσιάζονται στα Σχήματα 19-22.

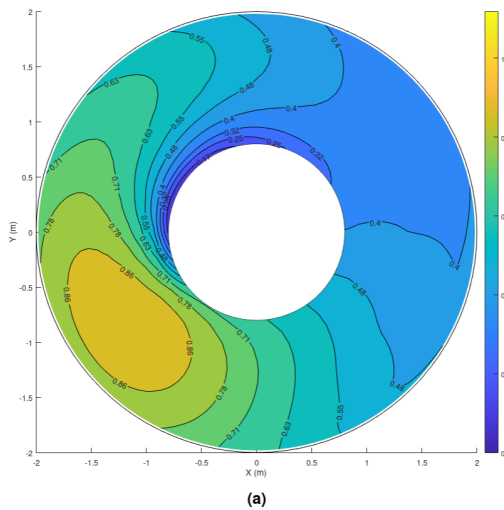
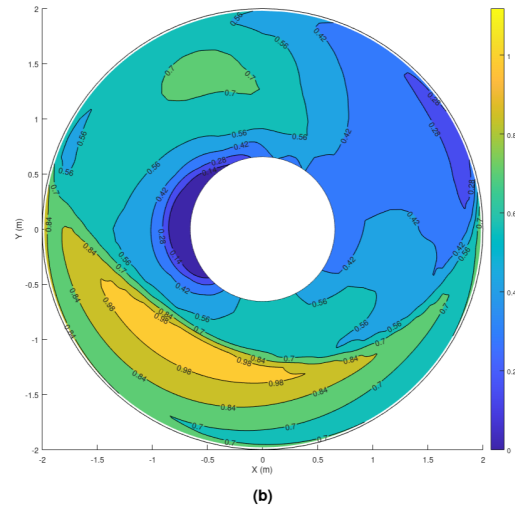
Επιπλέον, διαγράμματα για τις ίδιες μεταβλητές και λόγους προώθησης, ως συνάρτηση της αζιμουθιακής θέσης στην αδιάστατη ακτινική θέση $\bar{r} = 0.5$, παρουσιάζονται στα Σχήματα 23-24.

Μερικές γενικές παρατηρήσεις μπορούν να γίνουν:

1. Η ταχύτητα του ανέμου είναι ευθυγραμμισμένη με τον άξονα Ξ και κατευθύνεται προς τα δεξιά.
2. Το διάγραμμα της επαγόμενης ροής δείχνει ότι η εμπρόσθια περιοχή και η πλευρά πρόωσης ($0^\circ \leq \psi \leq 180^\circ$), παρουσιάζει μεγαλύτερη επαγόμενη ροή σε σύγκριση με την οπισθοχωρούσα πλευρά ($180^\circ \leq \psi \leq 360^\circ$).

(α') Peters-He για $M = 3$, $Q = 3$ 

(β') Μοντέλο γραμμής άνωσης

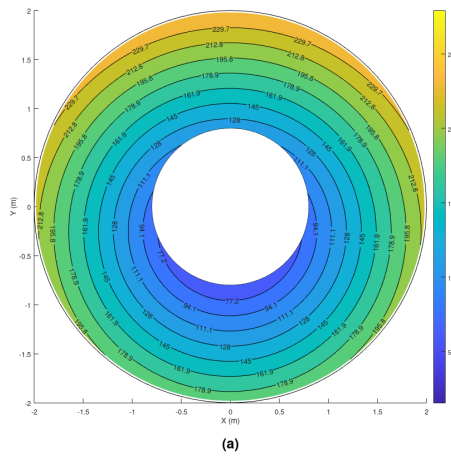
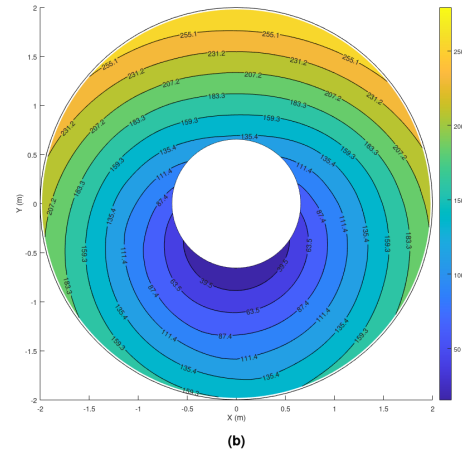
Σχήμα 15: BO-105 : Αδιάστατη επαγομένη ταχύτητα, w_{inflow} για $\mu = 0.26$ (α') Peters-He για $M = 3$, $Q = 3$ 

(β') Μοντέλο γραμμής άνωσης

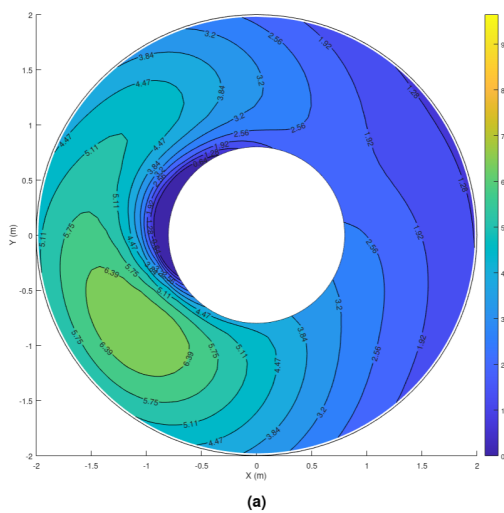
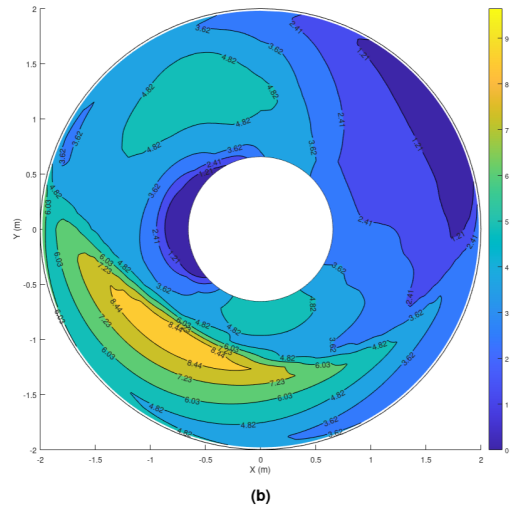
Σχήμα 16: BO-105 : Συντελεστής κάθετης φόρτισης C_N για $\mu = 0.26$

3. Όπως αναμενόταν, η ταχύτητα είναι σημαντικά μεγαλύτερη στην πλευρά πρόωσης και χαμηλότερη στην οπισθοχωρούσα πλευρά λόγω της περιστροφής του δρομέα.
4. Ως αποτέλεσμα της διαφοράς ταχύτητας, το διάγραμμα κατανομής της γωνίας προσβολής δείχνει ότι η πλευρά πρόωσης του ρότορα έχει μικρότερη γωνία προσβολής από την οπισθοχωρούσα πλευρά.

Από τα διαγράμματα, μπορεί να συμπεράνει κανείς ότι οι κατανομές, αν και δεν είναι ταυτόσημες, ακολουθούν ένα παρόμοιο μοτίβο. Το μοντέλο γραμμής άνωσης ελεύθερου ομόρρου προσφέρει μεγαλύτερη ακρίβεια και μπορεί να αποτυπώσει την επαγομένη ροή με μεγαλύτερη ακρίβεια, αλλά είναι χρονοβόρο και ακατάλληλο για εφαρμογές σε πραγματικό χρόνο. Ωστόσο, η κατανομή που προκύπτει από το μοντέλο προσομοίωσης Peters-He, αν και δεν αποτυπώνει όλα τα φαινόμενα,

(α') Peters-He για $M = 3$, $Q = 3$ 

(β') Μοντέλο γραμμής άνωσης

Σχήμα 17: BO-105 : Τοπική ταχύτητα U για $\mu = 0.26$ (α') Peters-He για $M = 3$, $Q = 3$ 

(β') Μοντέλο γραμμής άνωσης

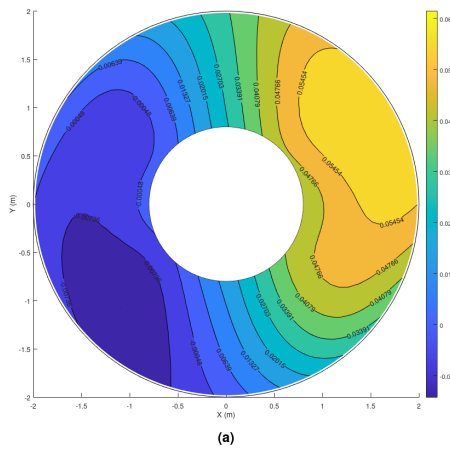
Σχήμα 18: BO-105 : Γωνία προσβολής α για $\mu = 0.26$

φαίνεται ικανοποιητική για τον σκοπό που προορίζεται.

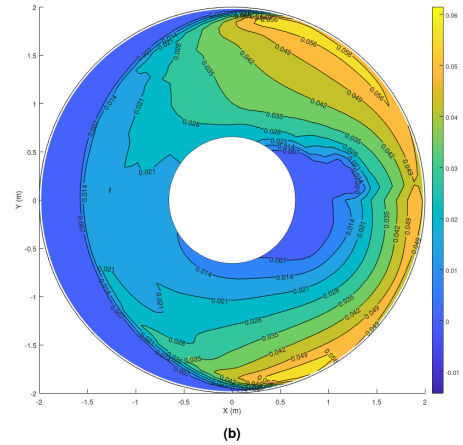
Εν κατακλείδι, σε αυτήν τη διπλωματική εργασία μελετήθηκε το μοντέλο ομόρρου πεπερασμένων καταστάσεων Peters-He, και αναπτύχθηκε ένας ανοιχτός κώδικας προσομοίωσης του μοντέλου αυτού. Για την αξιολόγηση της ακρίβειας του κώδικα, έγιναν συγκρίσεις με ένα μοντέλο γραμμής άνωσης ελεύθερου ομόρρου χρησιμοποιώντας τη γεωμετρία του ελικοπτερού BO-105.

Τα αποτελέσματα δείχνουν ότι το μοντέλο Peters-He προσφέρει σημαντικά πλεονεκτήματα σε σχέση με απλούστερα μοντέλα ομόρρου, ενσωματώνοντας υψηλότερες αρμονικές αποκρίσεις και καταγράφοντας πιο σύνθετη κατανομή του ομόρρου. Ωστόσο, η συμβιβαστική σχέση μεταξύ του υπολογιστικού κόστους και της ακρίβειας είναι εμφανής, αφού το μοντέλο Peters-He δεν επιτυγχάνει το ίδιο επίπεδο ακρίβειας με το μοντέλο γραμμής άνωσης ελεύθερου ομόρρου.

Επιπλέον, οι παραδοχές που έγιναν περί χρονικά ανεξάρτητων συνθηκών περιορίζουν την εφαρμογή του μοντέλου. Για παράδειγμα, για τη μοντελοποίηση ελιγμών θα χρειαστεί η ενσωμάτωση ενός δυναμικού όρου στις εξισώσεις για να πετύχει κανείς αποτελέσματα με την προαπαιτούμενη

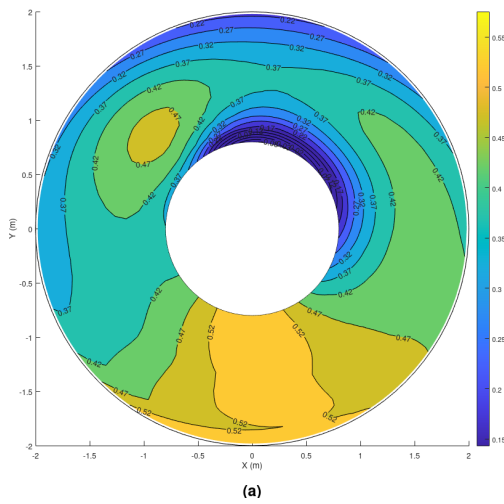


(α') Peters-He για $M = 3, Q = 3$

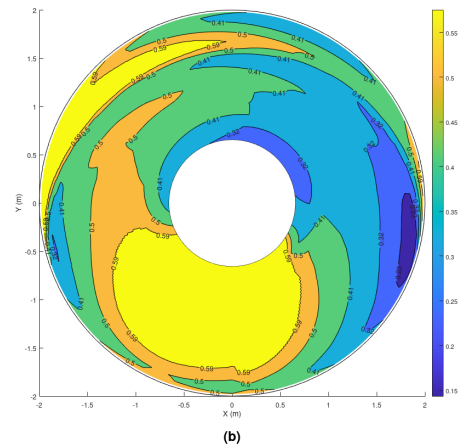


(β') Μοντέλο γραμμής άνωσης

Σχήμα 19: BO-105 : Αδιάστατες επαγόμενες ταχύτητες, w_{inflow} για $\mu = 0.13$



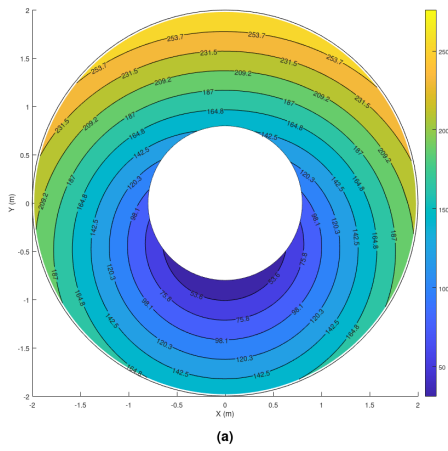
(α') Peters-He για $M = 3, Q = 3$



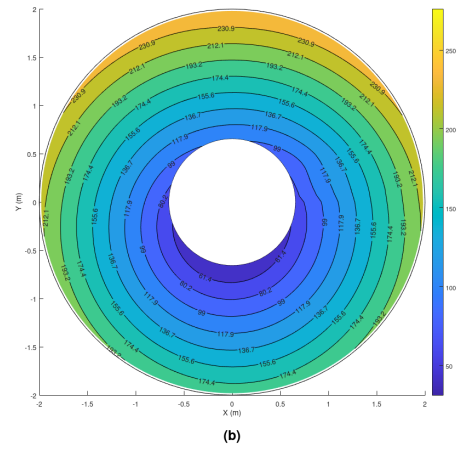
(β') Μοντέλο γραμμής άνωσης

Σχήμα 20: BO-105 : Συντελεστής κάθετης φόρτισης C_N για $\mu = 0.13$

ακρίβεια. Εντούτοις, ο κώδικας που αναπτύχθηκε για το μοντέλο Peters-He παραμένει κατάλληλος για πρακτικές εφαρμογές, ιδιαίτερα για προσομοιώσεις σε πραγματικό χρόνο, όπου απαιτείται ισορροπία μεταξύ ταχύτητας και ακρίβειας.

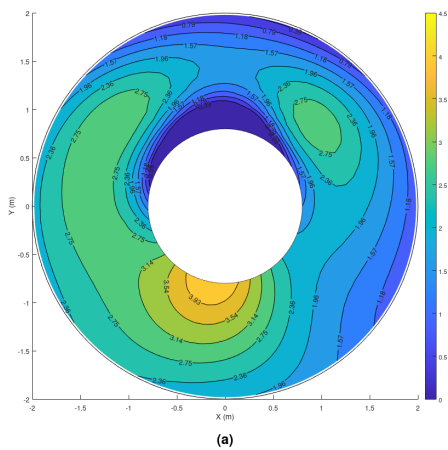


(α') Peters-He για $M = 3, Q = 3$

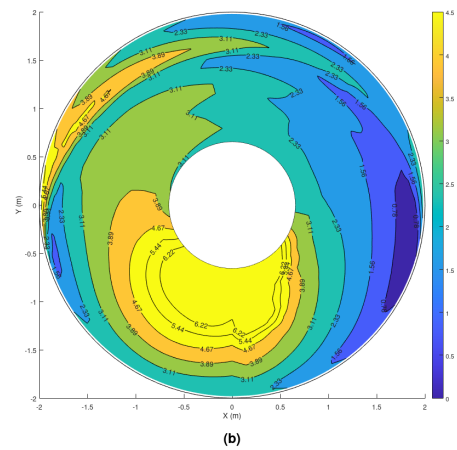


(β') Μοντέλο γραμμής άνωσης

Σχήμα 21: BO-105 : Τοπική ταχύτητα U φορ $\mu = 0.13$

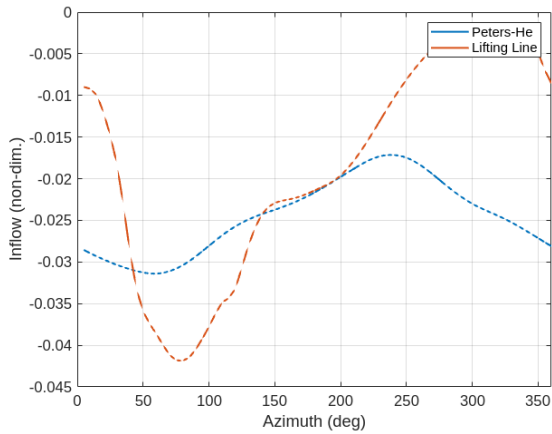


(α') Peters-He για $M = 3, Q = 3$

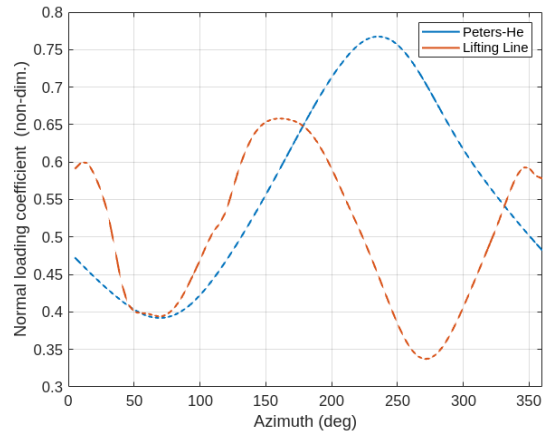


(β') Μοντέλο γραμμής άνωσης

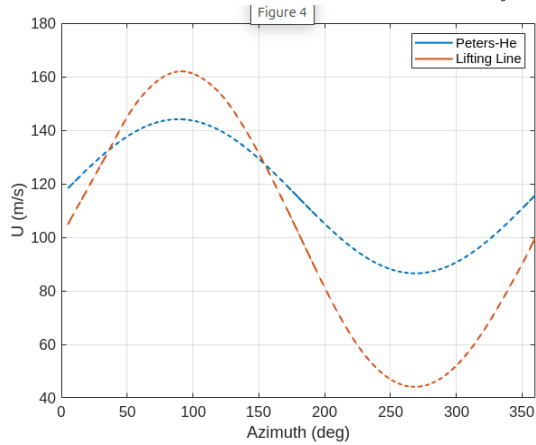
Σχήμα 22: BO-105 : Γωνία προσβολής α για $\mu = 0.13$



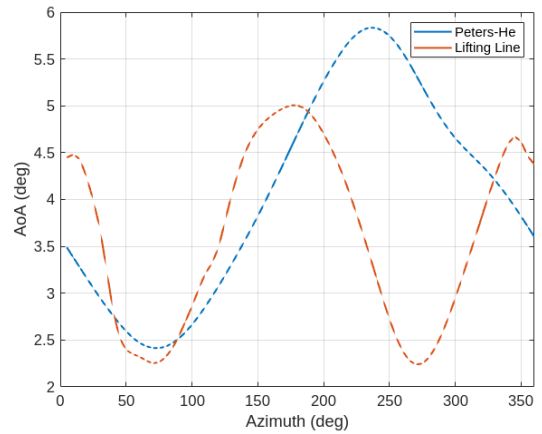
(α) Αδιάστατη επαγομένη ταχύτητα w_{inflow}



(β) Συντελεστής κάθετης φόρτισης C_N

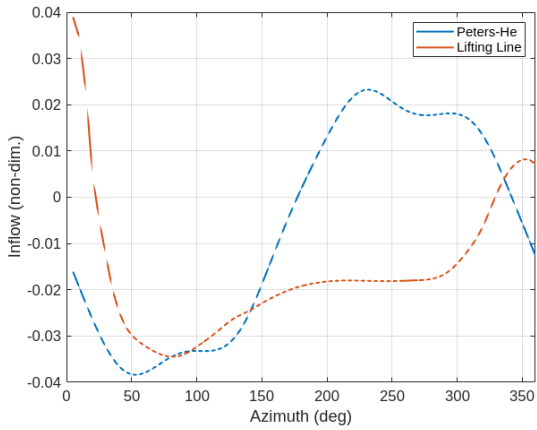


(γ) Τοπική ταχύτητα U

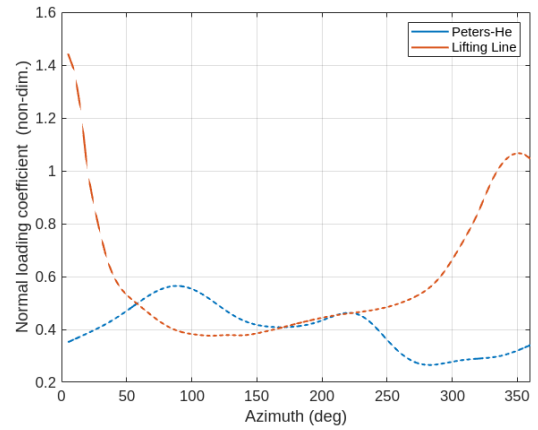


(δ) Γωνία προσβολής α

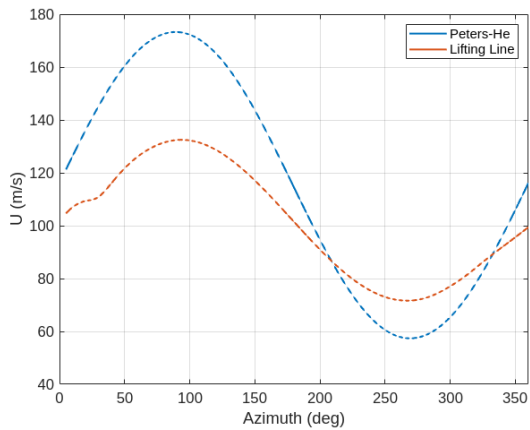
Σχήμα 23: Αποτελέσματα για $\mu = 0.26$ και $\bar{r} = 0.5$ ως συνάρτηση της αζιμουθιακής θέσης



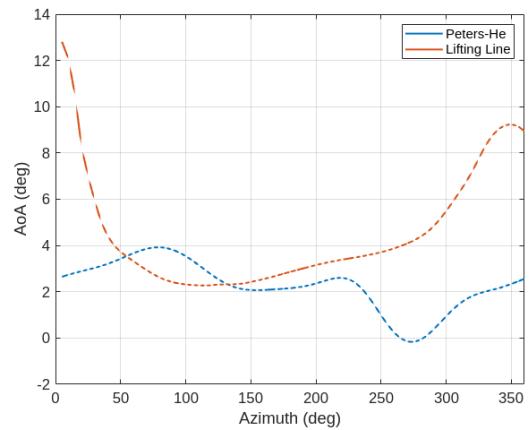
(α') Αδιάστατη επαγομένη ταχύτητα w_{inflow}



(β') Συντελεστής κάθετης φόρτισης C_N



(γ') Τοπική ταχύτητα U



(δ') Γωνία προσβολής α

Σχήμα 24: Αποτελέσματα για $\mu = 0.13$ και $\bar{r} = 0.5$ ως συνάρτηση της αζιμουθιακής θέσης